Immobilization of Gold Nanoparticles for Colourimetric and Ratiometric Refractive Index Sensing

by

Lori Pollit

A thesis
presented to the University of Waterloo
in fulfillment of the
thesis requirement for the degree of
Masters of Science
in
Vision Science

Waterloo, Ontario, Canada, 2019

AUTHOR'S DECLARATION

I hereby declare that I am the sole author of this thesis. This is a true copy of the thesis, including any required final revisions, as accepted by my examiners. I understand that my thesis may be made electronically available to the public.

Abstract

The development of refractive index sensors is an expanding field of research, with applications in fields including medical diagnostics, food safety and public health. Nanotechnology has become widely implemented in various refractive index sensing techniques, resulting in substantial progress in detecting minute changes of refractive index. A literature review of the current refractive index sensing techniques which incorporate nanotechnology demonstrates that two main strategies for refractive index sensors have been developed, those that provide highly sensitive measurements and those that provide visual colourimetric measurements that can be detected by the naked eye. All colourimetric sensors based on gold nanoparticles offer a red to blue shift, however, this thesis outlines the development of a ratiometric colourimetric refractive index sensor that provides a unique blue to red shift.

The development began with controlling the deposition of the various gold nanoparticle populations which are immobilized via electrostatic interactions between a weak polyelectrolyte and the gold nanoparticles. It was determined that by altering the pH of the polyelectrolyte as well as the size and concentration of the gold nanoparticles, modulation of the nanoparticle populations could be achieved. The nanoplasmonic surfaces were then shown to be effective sensors for the refractive index range of 1.00 to 1.47, providing both red to blue and blue to red colourimetric shifts, depending on the ratio of the different immobilized nanoparticle ensembles. The sensor surfaces were shown to be reusable, however the electrostatic interactions responsible for immobilizing the nanoparticles were weakened when exposed to various cleaning solutions and common solvents, resulting in nanoparticle loss from the sensor surface. Lastly, the optical response achieved by the refractive index sensors was simulated using COMSOL Multiphysics, which provided insight on the properties that resulted in the unique colourimetric shifts.

Acknowledgements

I would like to express my gratitude to my advisors Professor Lyndon Jones and Professor Frank Gu for their advice, guidance, support and resources throughout the development of my research project. I am also grateful to Paul Chen from the Frank Gu Lab, whose mentorship and guidance in designing the project was invaluable.

I would also like to extend my appreciation to all of the past and present members of the Frank Gu lab and CORE research group including Mahtab Roshandel, Michelle Si, Sukrit Rajpal, and Alan Yee who have helped me along the way and made my time enjoyable.

Finally, I would like to recognize the financial support I received from the Canadian Institute of Health Research (CIHR), Science Graduate Experience Award, Science Graduate Student Award, University of Waterloo Graduate Scholarship and the University of Waterloo President's Graduate Scholarship.

Table of Contents

List of Figures

List of Tables

List of Abbreviations

AFM: Atomic force microscope

APTES: (3-Aminopropyl)triethoxysilane

AuNP: Gold nanoparticle

BSA: Bovine serum albumin

CTAB: Cetyltrimethylammonium bromide

DMSO: Dimethyl sulfoxide

EOT: Extraordinary optical transmission

FBG: Fiber Bragg grating

LSPR: Localized surface plasmon resonance

nanoLCA: Lycurgus cup (nanofunnel)

PAA: Poly(acrylic) acid

PBS: Phosphate-buffered saline

PVT: Polyvinyl tetrazole

RIU: Refractive index unit

SDS: Sodium dodecyl sulfate

SEM: Scanning electron microscope

SPR: Surface plasmon resonance

List of Equations

Chapter 1
Introduction

1.1 Overview

Traditionally, refractive index measurements have simply been used to analyze material properties, however, through the incorporation of nanotechnology, substantial progress in the development of refractive index sensors has been achieved allowing them to be implemented in fields such as cancer detection[1]–[5] diagnosis of allergies[6], heavy metal detection in water[7], [8] and bacterial sensing[9]–[14]. With significance in these critical fields, the development of sensors to detect refractive index has become a rapidly expanding field of research, producing innovative and effective ways to optimize detection efficiency, cost per test and feasibility of worldwide implementation.

An area that remains less explored in the field of refractive index sensors is the development of nanostructured optical ratiometric sensing platforms, which measure the modulation between two or more optical outputs to provide refractive index measurements. Ratiometric sensors that have previously been developed use optical fiber-based or microfluidic-based detection techniques[15]–[18]. Inherent to these sensing designs, elaborate setups and external equipment are required to analyze the ratiometric outputs and therefore, are unable to be easily implemented onto common commercial products to passively provide on-site refractive index measurements. Nanostructures have potential to be implemented as ratiometric refractive index sensors on commercial surfaces, however these sensing mechanisms have currently been limited to theoretical simulations or modeling and have yet to be experimentally demonstrated[19], [20]. Therefore, a nanostructured ratiometric refractive index sensor that has potential to be implemented onto various surfaces for simple, immediate and on-site refractive index detection, without the aid of external equipment remains a challenge.

A versatile ratiometric refractive index sensor was designed that contains both single and clustered gold nanoparticles and provides an immediate colourimetric signal that can be detected by the naked eye. The deposition of the spherical gold nanoparticles is based on electrostatic interactions and can be tailored to be deposited on different surfaces as well as to vary the initial colour of the sensor surface. When exposed to an increase in refractive index, the ensemble of gold nanoparticles experiences a ratiometric optical response in extinction intensity, which results in a blue to red

colourimetric shift on the nanoplasmonic surface. This ratiometric response and consequent blue to red colourimetric shift has not been previously documented and therefore, determining the underlying cause of this unique occurrence would provide a valuable contribution to the current scientific literature on the implementation of gold nanoparticles in refractive index sensors.

1.2 Research Objective

This thesis focusses on the development and characterization of a ratiometric refractive index sensor that provides a novel blue to red colourimetric output using a stationary nanoplasmonic substrate. The ratiometric response originates from the deposition of various gold nanoparticle ensembles, which respond differently to changes in refractive index, thus creating a visually apparent ratiometric response. The optical properties of the nanoplasmonic sensor surface can be tailored based on the immobilization state of the deposited nanoparticles, which can be determined using a versatile immobilization method. The explanation behind the optical outputs experimentally achieved can be understood by recreating similar responses using simulations and studying the optical responses of the component ensembles. The specific objectives encompassed in the development and characterization of this ratiometric refractive index sensor include:

1. Immobilize colloidal gold nanoparticles onto a glass surface with a controllable, predictable deposition profile
    - Understand how surface properties can be used to control the deposition of the gold nanoparticles (i.e. degree of clustering)
    - Determine the effect on the optical surface properties when depositing different concentrations and sizes of gold nanoparticles
    - Characterize the colourimetric responses to refractive index changes with sensors containing various gold nanoparticle deposition profiles
2. Understand the abilities and limitations of the refractive index sensor
    - Test the reusability of the sensor surface
    - Test the effect of different environmental exposures on the immobilization state of the gold nanoparticles
3. Develop a mechanistic understanding for the ratiometric response on the nanoplasmonic surfaces

- Simulate component nanoclusters under various refractive index environments
- Utilize component simulations to determine the rationale behind the ratiometric optical response to refractive index changes
- Combine a representative portion of isolated and clustered simulated nanoparticles to achieve a similar optical response to that experienced experimentally

1.3 Thesis Outline

This thesis encompasses a chapter of literature review, three experimental research chapters and a chapter that discusses conclusions and recommendations for future work. The first chapter provides an overview of the structure and contents of this thesis as well as outlines the motivation and objectives of this research.

The second chapter provides a literature review on previously developed refractive index sensing mechanisms. The review focuses on sensors that harness the unique optical properties of nanomaterials and highlights the sensing principles used to gain refractive index sensitivity. This review also summarizes how these sensors have been incorporated into biosensing applications, emphasizing the increasing importance of refractive index sensing in biomedical fields.

The third chapter explores the development of a novel ratiometric refractive index sensor that immobilizes single and clustered gold nanoparticles on a functionalized glass substrate. By modulating the deposition parameters, the degree of single and clustered nanoparticle populations immobilized can be controlled, thus regulating the optical properties of the sensor. The resiliency of the nanoparticle immobilization to the exposure of various solutions and solvents was also tested to determine restrictions of the sensor for commercial implementation.

The fourth chapter provides a proof-of-concept for the ratiometric refractive index sensing capabilities of the nanoplasmonic surface developed in Chapter 3. Depending on the initial concentrations of isolated and clustered nanoparticles deposited, red to blue and blue to red colourimetric changes in response to refractive index changes were achieved. The sensor surface was also tested for reusability.

The fifth chapter analyzes simulations that have been conducted to theoretically confirm the optical properties of the sensor surfaces observed experimentally. By simulating the individual nanoparticles and nanoclusters that comprise the nanoplasmonic surface, the different contributions

from the various ensembles can be isolated and analyzed, providing an explanation as to how the ratiometric property of the sensor is achieved.

Lastly, the sixth chapter summarizes the results obtained from this research and presents recommendations for future work to improve the commercial viability of this sensor.

Chapter 2
Literature Review

2.1 Summary

Nanotechnology has allowed for unprecedented advances in refractive index sensors, which have been utilized in biomedical fields including medical diagnostics, food safety and public health. Refractive index simply describes how light propagates through a medium and is defined as the speed of light in a vacuum divided by the phase velocity of light in a medium. However, with the substantial progress made in detecting minute changes in refractive index using nanomaterials, refractive index sensors have become powerful tools exploited in various biosensing applications. Here, refractive index sensors that utilize nanostructures are reviewed, providing an emphasis on the descriptions of the sensing mechanisms and their versatility to be employed as biosensors.

2.2 Introduction

Since the initial conception of refractometers in the 1880s and 1890s, the functionality of refractive index measurements has expanded beyond the determination of how light propagates through a medium. With the inherent sensitivity of refractive index on various physical and optical properties of a medium, refractive index measurements can be used to determine a broad range of information about a material, as well as its local environment[21]–[24]. In particular, there has been a growing interest in using refractive index measurements to determine the presence of biological analytes based on their unique refractive index profiles. Therefore, refractive index detection has gained popularity in the field of medical diagnostics, food safety and public health. Sensors employed in these fields generally trend towards providing user friendly and equipment-free optical outputs for

on-site measurements of bulk solutions or providing highly sensitive and specific measurements able to detect single cells or bacteria in a clinical or laboratory environment. The former commonly uses colourimetric outputs that are discernable by the naked eye, whereas the latter often uses non-colourimetric sensors that utilize prisms or optical fibers. Depending on the specific requirements of the biosensing application, there is a wide range of techniques that can be employed to provide the desired refractive index measurement.

As fabrication techniques for intricate nanostructures and uniform nanofilms become more efficient and economical, the unique optical properties of various nanomaterials are becoming widely adopted to create new refractive index sensors or enhance existing sensing techniques. The inherent refractive index sensitivity of metal nanomaterials is imparted by their free electrons, which can be resonantly excited by light to generate surface plasmon oscillations. Based on the architecture of the nanostructure, these oscillations can experience different types of plasmon resonances when exposed to light such as surface plasmon resonance (SPR) and localized surface plasmon resonance (LSPR). Briefly, SPR is the oscillation of conduction electrons at the interface of two materials, commonly a metal and dielectric material, whereas LSPR is the oscillation of conduction electrons from metal nanoparticles. The resonant frequencies of these oscillations are sensitive to the local refractive index and therefore, shifts in these frequencies provide a means to determine shifts in refractive index. With the inclusion of these nanomaterials in refractive index measurements, unparalleled advancements have been made in refractive index sensing and have been applied in fields ranging from bacterial sensing to cancer cell detection[6], [9]–[12], [25], [26].

This brief review aims to explore the most recent and commonly implemented nanomaterial-based refractive index sensing techniques, with a view to understanding the mechanisms by which refractive index sensitivity is achieved. Sections are separated based on the sensing platform used, and focus will be given to how the sensors have been applied in biosensing applications.

2.3 Refractive Index Sensors

2.3.1 Kretschmann Configuration-Based Sensors

A specific type of SPR-based refractive index sensor is the Kretschmann-type SPR sensor, which utilizes plane-polarized light, a prism containing a thin metal film, as well as a photodiode detector (Figure 1). In this sensing mechanism, p-polarized light passes through the prism and is subjected to total internal reflection at the thin metal film transducer surface, commonly a gold film,

50 nm thick. At a certain angle, known as the resonance angle or the SPR angle, the light reflected from the prism/transducer interface is attenuated. This attenuation occurs due to the resonance between the excited plasmon wave produced from the gold film and the evanescent wave created from the incident light. Since the evanescent wave extends into the local environment and is sensitive to the local refractive index, changes in the environmental refractive index correspond to changes in the SPR angle. Therefore, a shift in the angle of light exiting the prism can be correlated to changes in the local refractive index experienced by the gold film.

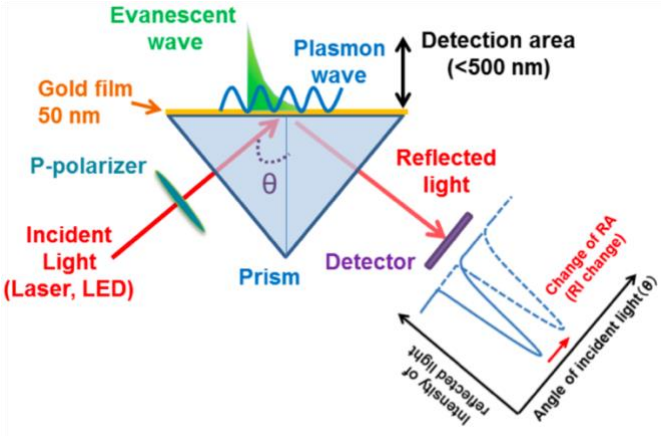

Figure 1. Principle of a Kretschmann-type SPR sensor to detect refractive index changes on a gold surface. Reprinted with permission from Yanase et al., [6] **copyright 2016 Optical Society of America.**

Kretschmann-type SPR refractive index sensors have historically provided a sensitivity on the order of 5 x 10^{-7} degree/RIU[27], however there has been many advancements in optimizing the transducer surface to increase the sensitivity. Modifications to the transducer surface often include replacing the continuous metallic film with nanostructures, which provide an increased active surface area as well as local field enhancements[28]. A selection of these nanostructures implemented on the transducer surface are reviewed here, however comprehensive reviews of these advancements can be found in these excellent reviews[28]–[30].

Gold and silver are commonly employed metals used for the transducer surfaces, both offering unique advantages. When comparing the two materials, silver provides a sharper SPR resonance peak whereas gold provides better sensitivity, bandwidth and resistance to oxidation and corrosion[28]. Therefore, gold has been more frequently chosen for implementation into refractive index sensors[6], [9]–[12], [26]. However, advancements in silver transducer surfaces have shown

that using a porous metallic film consisting of silver ellipsoidal nanostructures, provided increased environmental stability[31] and enhanced sensitivity by a factor of 3 compared to a silver continuous film. Another modified silver transducer surface was developed where the upper surface exposed to the environment contained a nano-sized grating structure with periodic troughs and peaks[32]. When light passed through the prism and reflected off the prism/silver interface, the evanescent field penetrating the silver film coupled to the surface plasmon on the grating side of the silver film. This design created almost a 6-fold increase in refractive index sensitivity when compared to the sensor which only used a smooth silver film. However, this was not specific to a silver transducer, as similar results were achieved when applying this grating structure to a gold transducer[33]. In addition to modifying the structure of the transducer surface, it was demonstrated that combining layers of gold and graphene in the transducer surface, only a few nanometers thick, improved refractive index sensing for the detection biological analytes[34]. The improved sensitivity originated from the π-stacking interactions amongst the hexagonal graphene cells and the carbon-based ring structure in the biological analyte. However, a broader and shallower SPR reflectance curve as well as a decrease in detection accuracy was also experienced with the graphene layers, as they dampened the surface plasmons from the gold. Therefore, the higher sensitivity came with a trade-off for detection accuracy and spectral width of the SPR curve.

The Kretschmann-type SPR sensor has been implemented for biosensing applications by functionalizing the transducer film with biorecognition elements. The device SPREETA™, made by Texas Instruments, utilizes this SPR phenomenon, providing a portable, economic and rapid biosensor that has been applied for bacterial sensing[9]–[12]. In addition to detecting the presence of certain analytes, this sensing technique can be used to detect biological changes in living analytes that coincide with refractive index changes[6], [25], [26]. This was utilized for cell-based diagnosis of allergies and cancer[5],[7] as well as understanding how cells respond to toxins[25]. However, when using this technique to measure biological analytes, intrinsic factors that limit SPR detection include the resemblance of the refractive index of the analyte to the external medium[11] as well as the sensitivity of the resonance angle to the film thickness, where surface inconsistencies such as analyte aggregation compromise measurements[9]. Additionally, the sensing SPR electromagnetic evanescent field experiences exponential decay and consequently has a very restricted penetration depth through which it can detect surface analytes[11]. Therefore, when detecting refractive index changes induced by larger biological analytes such as bacteria, employing shorter binding ligands is preferred, as it

allows for a larger proportion of the analyte to be within the SPR range, providing better detection sensitivity.

Overall, despite this measurement technique being developed almost 4 decades ago, it still remains a focus of current research. With the known benefits of incorporating nanomaterials into the foundation of the sensor design, it is likely that nanostructured modifications will continue to be studied such that this fast and inexpensive sensing platform could perform clinically relevant biosensing analysis in both laboratory and field settings.

2.3.2 LSPR-Based Sensors

The rise in the popularity of fabrication techniques such as lithography, ion etching, and electron beam evaporation has allowed for a wide expansion of unique nanosized architectures exploited for refractive index sensing. Commonly, nanostructures are organized into arrays and gratings, which can provide colourimetric optical outputs in response to refractive index changes. These sensing platforms are based on localized surface plasmons generated at the nanostructured grating surfaces. The LSPR wavelengths experience a red-shift when exposed to an increased refractive index, often demonstrated as a shift in reflectance peak as well as a visual colour change of the grating surface (Figure 2A and 2B). With the ability to provide a discernable visual output, these sensors can be designed for immediate on-site detection, and benefit from the absence of external equipment to analyze the optical signal.

There have been significant research efforts developing unique nanostructures to enhance the LSPR sensitivity to local refractive index changes. Examples of nanostructures that were recently exploited for refractive index sensing include arrays of nanoforests[35], nanomushrooms[36],[37], nanoumbrellas[38], nanotriangles[13], nanosquares[39], nanodisks[1], nanorods[40],[41], nanopillars[42],[43], nanospheres[44],[14], nanomarbles[2], nanohemispheres[45] as well as nanowire gratings[46] (Figure 2A-2F). This sensing platform was able to provide sensitivities as high as 2508 nm/RIU[36] with customizable initial colours through altering the size[35],[39] or pitch[46] of the nanostructures. However, not all sensors provided simplistic colourimetric shifts from one visible colour to another. In response to an increase in refractive index, a sensor incorporating aluminum nanowire gratings experienced a resonant peak shift from visible wavelengths to invisible wavelengths, thus switching from a bright coloured state to a dark state[46]. Furthermore, rather than detecting the refractive index of the analyte itself, a sensor was designed containing a protein functionalized on the plasmonic surface, whereby in the presence of a specific analyte, the protein

underwent a conformational change, altering the refractive index experienced by the plasmonic surface[40]. This sensing technique created the potential for large optical signals to be experienced by small analytes that would otherwise not individually stimulate a large optical signal. Another signal amplification method exploited the formation of metal-organic-framework crystals on the captured analytes, which increased the change in refractive index and amplified the LSPR shift experienced by the nanostructures[41]. However, when employing nanostructures for LSPR-based refractive index sensing, not all nanostructures were organized in arrays or gratings, and some were suspended in aqueous solutions. This was seen with gold nanobipyramid structures, which combined LSPR sensing with surface enhanced Raman scattering and able to provide a limit of detection of 10^{-12} M based on refractive index[47].

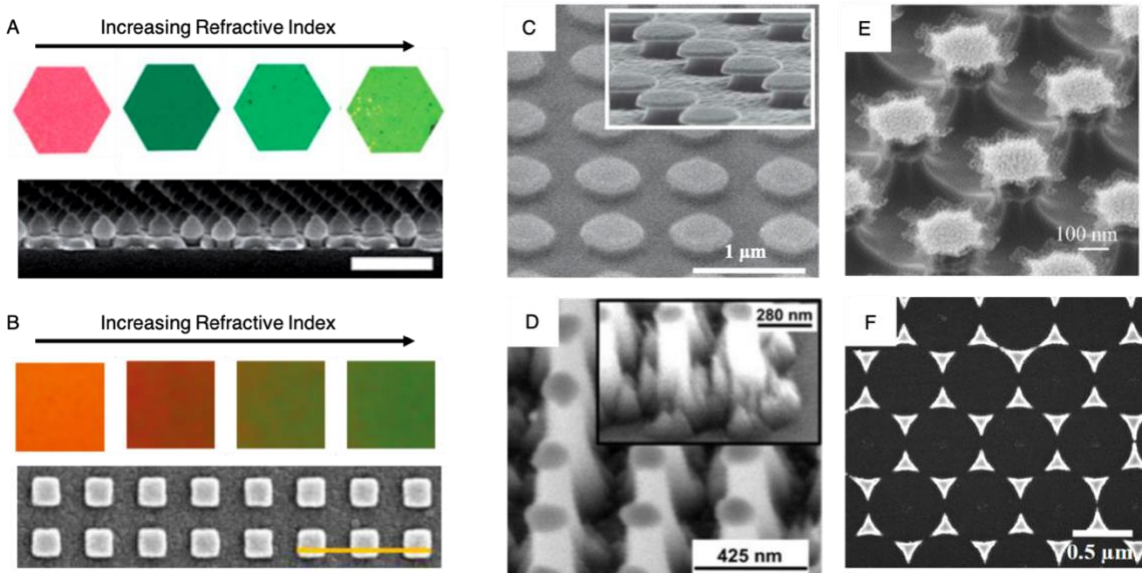

Figure 2. (A) Optical microscopy images of a gold nanoforest array to demonstrate reflected colour sensitivity to refractive index (top). SEM image of the gold nanoforest surface (bottom). Scale bar is 1 µm. (B) Brightfield images of a gold grating surface to demonstrate reflected colour sensitivity to refractive index (top). SEM image of the gold grating surface (bottom). Scale bar is 1 µm. (C-F) SEM images of (C-D) gold nanomushroom arrays, (E) gold nanoumbrellas arrays, and (F) gold nanotriangle arrays used in refractive index measurements. Reprinted with permission from (A) Heo et al.,[35]**, copyright The Royal Society of Chemistry 2012; (B) Khorasaninejad et al.,**[39] **copyright 2013 IOP Publishing Ltd; (C) Bhattarai et al.,**[36] **copyright 2015 Wiley-VCH Verlag GmbH & Co. KGaA Weinheim; (D) Bhalla et al.,**[37]

copyright 2017 American Chemical Society; (E) Fan et al.,[38] **copyright 2016 Elsevier; (F) Hu et al.,**[13] **copyright 2017 American Chemical Society**

These sensors have potential in point-of-care and home health care diagnostic applications, as refractive index changes of bulk solutions can often be detected by the naked eye[16],[19],[26],[30],[31]. LSPR plasmons generally have a penetration depth from 5 nm to 30 nm, which provides an optimal range to analyze biological monolayers[48]. Although utilizing LSPR sensing techniques to detect bacterial species has been limited when using antibodies[49], aptamers have been successfully employed to capture and detect whole bacteria, with detection limits down to 30 cfu/assay[14] and detection ranges of 10 to 10_3 cfu/ml[13]. These sensors also demonstrated the ability to specifically detect various bacterial species in a multiplexed mode[14] and remain functional after being stored over 2 months in ambient conditions[13]. Furthermore, applications can be found in pre-biopsy tests for cancers, by detecting cancer specific antigens[1] and epithelial cell adhesion molecules expressed on cancer cells[2]. To specifically detect cellular secretions, one particular sensor utilized gold nanopillars on a substrate containing microwells designed to capture cells. This allowed the nanopillars to detect secretions from the trapped cells with a detection limit of 10 ng/μL for the secretion of anti-IgA[42]. Hydrogels have also been implemented in LSPR refractive index sensors, either as a means to electrostatically attract analytes of interest to the plasmonic nanostructures[50], or as a means of immobilizing the nanostructures while the analytes reach the active surfaces via diffusion[51]. These techniques were seen to detect protein biomarkers for chronic dry eye[50] as well as BSA molecules[51].

These sensors provide a promising means for user-friendly, on-site refractive index analysis; however, these sensing platforms experience several tradeoffs. Certain sensor designs require that specific viewing angles are maintained to see the colour change with the naked eye[52]. Additionally, in the colourimetric sensor designs discussed in this section, to produce a visually discernable optical output, bulk sample volumes are required, limiting the scope of the applications. Research has been conducted to amplify output signals; however, future work is required to apply the technology for the visual detection of microscopic analytes.

2.3.3 Diffraction-Based Sensors

When light interacts with vertical nanowires or nanopillars, it experiences a degree of diffraction (Figure 3A and 3B) which is dependent on the refractive index of the local environment and contributes to the apparent colour of the nanostructured surface (Figure 3C). This allows arrays of

nanowires or nanopillars to be exploited as colourimetric refractive index sensors. This sensing principle is understood through Bragg diffraction theory, which explains how a visual output correlated to refractive index can be achieved through a change in diffraction[53]. Bragg diffraction theory states that when light interacts with a periodic assembly and is incident along one of the lattice directions, diffraction occurs, and the light is redirected. When the light is sent in a direction which has a path length difference of an integer multiple of the incident wavelength, constructive interference occurs. The path difference of light from neighbouring nanostructures d nm apart is given by $d(n_1 \sin\theta_i \pm n_1 \sin\theta_r)$, where n_1 is the local refractive index of the medium, θ_i is the incident angle, and θ_r is the diffracted angle. Since the path difference is dependent on the refractive index, which in turn determines the wavelengths that undergo constructive interference and determines the colours generated, refractive index changes can be directly correlated to colourimetric shifts.

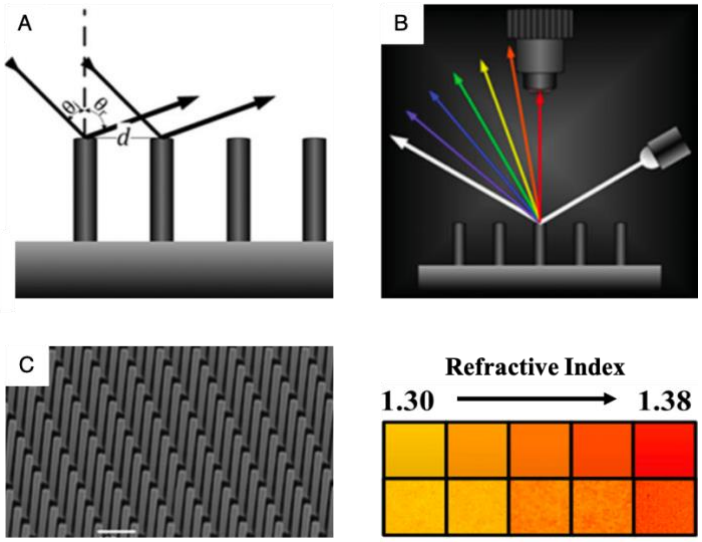

Figure 3. (A) Representation of simple Bragg diffraction from a periodic structure. (B) Experimental setup to observe diffracted colours from silicon nanowires. (C) SEM image of silicon nanowire array, scale bar is 600 nm (left). Theoretical and experimental colours observed when the silicon nanowire array is exposed to increasing refractive index (right). (A-C) Reprinted with permission from Walia et al., [53] **copyright 2013 Wiley-VCH Verlag GmbH & Co. KGaA, Weinheim.**

Vertically oriented nanowires and nanopillars fabricated from silicon[53]–[55] and polyvinyltetrazole (PVT)[7],[8] have been implemented as colourimetric refractive index sensors.

With regards to the silicon nanowires and nanopillars, silicon was selected as a preferred material as it contains a much larger refractive index than air and therefore provides vivid diffraction-based colours for refractive index ranges between 1.3 to 1.8[53] or 1.9[54]. Through the higher order diffraction modes, refractive index resolution on the order of 10^{-5} was achieved[55]. This diffraction-based refractive index sensing was also utilized to detect specific analytes, as demonstrated with PVT polymer pillars. These nanopillars exhibited selective adsorption of specific high refractive index metal ions such as lead[8] or chromium[7] ions which are both harmful to human health and highly desirable to detect[56]–[58]. The adsorbed metal ions increased the effective refractive index of the PVT brushes and it was seen that the chromium also caused the collapse of the PVT brushes, further contributing to the increase in effective refractive index. This corresponded to a diffraction induced colourimetric shift, thus providing the ability to detect lead or chromium at relevant concentrations designated by the World Health Organization and Environmental Protection Agency.

2.3.4 Nanohole Array-Based Sensors

2.3.4.1 Extraordinary Optical Transmission Sensors

With advancements in focused ion milling and imprinting nanofabrication methods, periodic arrays of nanosized apertures containing unique and unusual optical properties have been developed. Through classical physics, it is expected that the intensity of light transmitted through an aperture in an opaque metal sheet should decrease with decreasing aperture area. This theory was confirmed in the 1940s[59] and believed to be true up until 1998, when contradictory data was presented[60]. It was demonstrated that light with wavelengths larger than the diameter of the apertures in a metallic film were transmitted through the apertures at unexpectedly high intensities[60]. Furthermore, it was seen that more light was transmitted through the apertures than was incident on the aperture. Thus, the metal array of nanoholes played an active role in funneling the light through the film, rather than simply acting as a passive barrier[60]. This optical phenomenon came to be known as “extraordinary optical transmission (EOT)”.

Many reports have published detailed theories providing explanations for this unique optical phenomenon[61][62], and models have been developed to understand this phenomenon on a microscopic level[63]. These reports provide a general consensus that the excitation of surface plasmons helps channel light through the apertures and thus provides the EOT effect. The

wavelengths of light transmitted through the apertures are correlated with the refractive index of the local environment[63], therefore a change in the refractive index causes a shift in the EOT transmission peak and apparent colour of the substrate[64]. This measurable transmission spectrum shift allows EOT-supporting substrates to be employed as refractive index sensors, providing colourimetric outputs for refractive index changes.

The EOT optical phenomenon has been employed with varying nanohole-based arrays, including circular apertures[61],[5] (Figure 4A and 4C) and cross shaped apertures[65] (Figure 4B). The cross shaped metal apertures imparted polarization dependent characteristics on the array and allowed for the detection of refractive index changes as small as $1x10^{-3}$ RIU with the naked eye[65]. Furthermore, based on the period of the nanohole arrays, the initial colour of the surface could be altered (Figure 4C). For biosensing applications, EOT plasmonic substrates have been employed in microfluidic devices whereby the solution of interest is flowed across the sensing surface containing a biorecognition element to capture the specific analyte and consequently, detecting the presence of the analyte with the change in refractive index (Figure 4D). This strategy was shown to provide multiplexed detection and detect different bacterial pathogens in spiked urine samples by containing nanohole subdivisions functionalized with different antibodies (Figure 4E)[66]. The EOT sensing platform was also employed to monitor bacterial growth, requiring less than 100 bacteria on the sensor surface to provide a notable resonance wavelength shift[67]. Furthermore, EOT plasmonic substrates were also used to detect a breast cancer specific antigen, for tumor diagnostics[3].

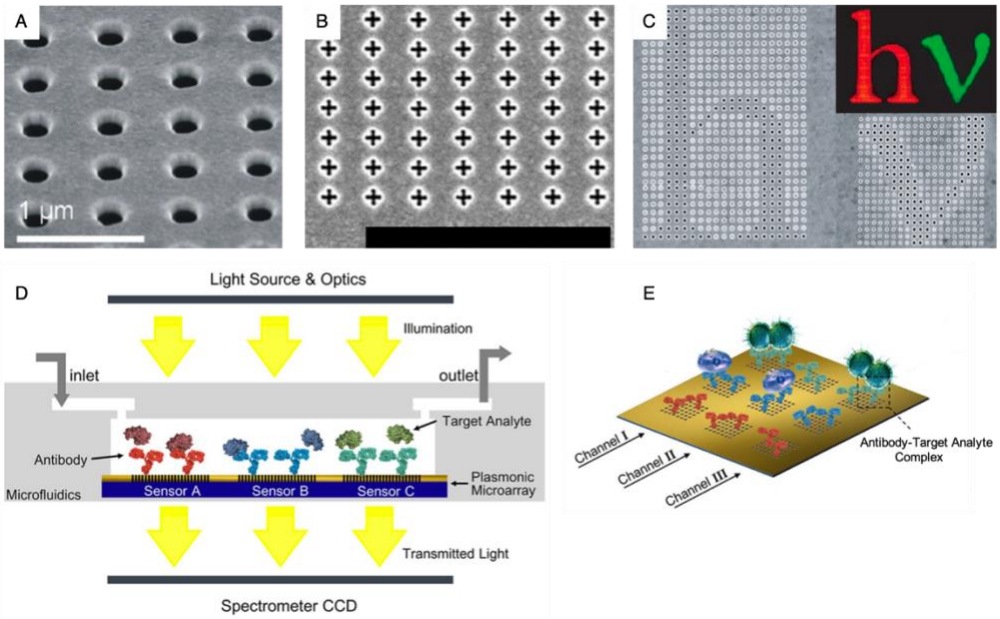

Figure 4. (A-C) Nanohole arrays fabricated by focused ion beam milling. (A) SEM image of circular nanohole array and (B) SEM image of cross-shaped nanohole array, scale bar is 2.5 µm. (C) Dimple array containing only select holes milled through. Initial colour of array shown to be dependent on the period of these nanohole arrays. Periods of 550 nm and 450 nm create initial colours of red and green respectively. (D) Overview of multiplexed EOT biosensor, functionalized with various antibodies to detect different bacteria. (E) Overview of the multiple channels contained in the sensor surface allowing for multiplexed detection. Reprinted with permission from (A) Escobedo, [5] **copyright The Royal Society of Chemistry 2013; (B) Langley et al.,** [65] **copyright Society of Photo-Optical Instrumentation Engineers (SPIE) 2016; (C) Genet et al.,** [61] **copyright Nature Publishing Group; (D-E) Soler et al.,** [66] **copyright 2017 Published by Elsevier**

2.3.4.2 Nanocup and Nanofunnel Sensors

A refractive index sensor which utilized a modified-EOT substrate was developed using gold plasmonic nanocup arrays[68]–[71], also referred to as Lycurgus cup (nanofunnel) (nanoLCA)[70],[71]. Rather than contain arrays of nanoholes in opaque metal films, these arrays were imprinted into plastic substrates. To facilitate plasmonic activity, the imprinted substrates were coated with a layer of metal, creating metal nanoparticles along the sides of the walls in the nanocup structures. Unlike traditional EOT substrates, which have multiple transmission peaks, the metal

nanoparticles deposited in these arrays experience plasmon scattering modes, which allow a single peak wavelength to be selectively transmitted through the structure, providing a simpler detection analysis. The transmitted wavelength depends on the local refractive index, providing colourimetric shifts and a reported sensitivity up to 4.6×10^4 nm/RIU[70]. Furthermore, these nanocup structures only require nanoimprint and electron beam deposition fabrication techniques. These are less expensive, less time consuming and provide higher throughput than electron beam lithography and focused ion beam milling commonly used to create traditional nanohole EOT surfaces in metal films.

These plasmonic nanocup arrays demonstrated their biosensing capabilities by providing a colourimetric response to a refractive index change induced by BSA/anti-BSA immune complex formations[72], as well as the adhesion of a single cell[68]. When analyzing the colour changes produced by a single cell, a brightfield microscope was required to image the colour change. By using fast frame rates on the brightfield microscope, this sensing technique provided real time measurements to analyze the cellular activity such as cellular migration, differentiation and detachment. An intrinsic limitation to this technique was that the quantity of cells monitored simultaneously was limited by the field of view of the microscope, however it provided a means to analyze cellular behaviour when exposed to various biochemical and biophysical stimuli. Furthermore, a sensing platform using these nanoLCA structures was incorporated into a portable smartphone-based sensing platform that incorporated an internal reference sample[71]. With the inclusion of reference colours when imaging the samples, the analyte of interest was less effected by the light source, filter algorithm, as well as light sensitivity of the camera. In addition to biological analytes, this sensing platform was used to detect explosive materials such as 2,4,6-trinitrotoluene, commonly known as TNT, which is desirable to detect in the field of public security[69].

2.3.4.3 Flow-Through Nanohole Sensors

As nanohole array-based refractive index sensors were initially developed, it was assumed that the top metal surface of the array provided the majority of the plasmonic signal. However, this was challenged in 2009 when it was established that the in-hole surface played the dominant role in the refractive index sensitivity[73]. It was demonstrated that a conventional nanohole array had a sensitivity of around 400 nm/RIU, however when the top surface was covered with silicon oxide, the sensor achieved a sensitivity of 650 nm/RIU. Therefore, the nanochannels created by default when fabricating nanoholes were the most plasmonically active. This initiated a distinction between

nanohole array-based sensors being either flow-over or flow-through, depending on whether the analytes passed over the top of the substrate or through the nanoholes.

In depth comparisons between flow-through and flow-over nanohole arrays were calculated using scaling analysis and numerical simulations[74]. The main overarching conclusions were that the flux of analyte to the sensing surface and the time response were substantially more efficient in flow-through sensors, which was supported in multiple experimental comparisons[52],[64],[65]. With the newly discovered benefits of flow-through sensors, nanohole channels were functionalized with biorecognition elements, integrated into microfluidic devices and used in biosensing applications. Flow-through devices were implemented to detect the real time adsorption of an ovarian cancer biomarker specific monoclonal antibody[5], live viruses[77], uropathogenic Escherichia coli[78], a cytotoxic protein secreted by Staphylococcus aureus[79] as well as a breast-cancer specific protein[4]. Furthermore, these sensors have been used to capture virus-like particles and analyze the efficacy of virucidal drugs by detecting virucidal peptide-induced particle rupture[80].

Since these nanochannels are exposed to fluid transfer, the substrate underlying the metallic film must have sufficient mechanical strength to support the applied fluid forces. Examples of the substrate materials that were employed were silicon nitride[65],[66],[68],[71], porous silicon membranes[75] as well as a polycarbonate filter membranes[4]. The polymer membrane provided a sensitivity lower than the other substrates, only achieving a maximum of 117 nm RIU^{-1}, however it did achieve a resolution of 4.1×10^{-5} RIU showing it was still sufficient for biosensing applications and did not require cleanroom fabrication[4]. However, to utilize these sensors in point-of-care diagnostics, the sensing platform and requisite instrumentation must be integrated into a portable device. Consequently, there has been a progression towards commercially available components with straightforward circuitry[82], including analogue smartphone components[83]. However, there is still room for expansion in the development of internalized pumps as most optofluidic sensors using this sensing platform have used external pumps to transport fluids to the sensing surface. In the field of microfluidic sensors, there have been pumps designed whereby the fluidic transport was initiated by a pressing force from a human finger[84]. Therefore, there is potential for these microfluidic sensors to be utilized in portable refractive index sensors for on-site biosensing applications.

2.3.5 Optical Fiber Grating-Based Sensors

Optical fiber gratings have also been an evolving area of research for refractive index sensors and have utilized various forms of nanomaterials to enhance the sensitivity of the refractive index

measurements. An optical fiber grating consists of a diffraction structure in a single-mode fiber containing a core with a periodically modulated refractive index. When light propagates through an optical fiber containing a fiber Bragg grating (FBG), once the incident light reaches the grating structure, specific wavelengths are reflected back, while the remaining light is transmitted through. The wavelengths that are transmitted and reflected depend on environmental and intrinsic properties of the fiber, such as temperature and strain, thus allowing its optical response to be used as a sensor for these properties. However, to enable refractive index sensitivity, an evanescent field must be emitted from the fiber, parallel to the fiber axis, and interact with the local environment. This interaction can occur at the cladding/environmental interface or the fiber/environmental interface. To create a fiber/environmental interface, cladding layers must be removed at the location of the grating, which can be done through etching[85] and polishing[86]. Additionally, by imprinting the FBGs in microfibers with diameters on the order of a few micrometers, the evanescent waves intrinsically extend beyond the fiber, also resulting in interactions with the local environment[87],[88]. With the evanescence field interacting with the local environment, the spectral position of its resonance depends on the effective refractive index. Therefore, changes in resonance wavelength can be measured to determine the refractive index of the local environment. Utilizing this sensing mechanism, optical fibers have been extensively used to detect refractive index changes based on the wavelengths of light that are attenuated and transmitted through the fiber[89]–[97], as well as wavelengths that are reflected[98]–[103].

In these optical fiber devices, the refractive index sensitivity is reliant on the diameter of the fiber containing the grating, where a lower diameter provides a higher sensitivity. Therefore, a sensor with a higher sensitivity experiences the drawback of increased fragility and inconvenient handling. Inherent to this sensing principle, the evanescent field experiences exponential decay as it moves away from the active interface. Consequently, the refractive index sensitivity is highly dependent on the penetration depth of the evanescent field. To increase this penetration depth, nanometer thick coatings which have a higher refractive index than the fiber cladding have been deposited. These coatings help transfer the resonant wavelengths into the coating, pulling them towards the external environment, and thus increasing the interaction with local refractive index[104]–[109]. Another technique used to increase penetration depth is through surface plasmon resonance. By depositing a thin metallic layer, the core-cladding coupling produces SPR cladding modes whose attenuation is sensitive to the refractive index of the local environment, thus providing a refractive index sensor (Figure 5A) [110],[111]. Furthermore, fiber gratings with microstructured optical fibers were used to

provide enhanced refractive index measurements (Figure 5B)[112]–[114]. Microstructured optical fibers contain a series of holes in the fiber cladding, and have been demonstrated to create an internal microfluidic channel[114]. This allows the evanescent field to interact with the liquid passing through the holes, providing accurate measurements with small volumes of liquid.

For biosensing applications utilizing optical fiber gratings, nanocoatings have been employed to enhance the sensitivity and provide lower detection limits of specific analytes of interest such as anti-IgG [106][115], C-reactive protein[116], protein concanavalin A[117] and ammonia[118] (Figure 5C and 5D). With the applied nanocoatings, measurements could be made in the clinical range with limits of detection as low as 10^{-11}M[106]. These sensors have also been applied for the detection of bacteria[119]–[122], achieving detection sensitivities up to 1929 nm/RIU[118] and able to detect concentrations as low as 10^2 CFU/ml[122]. A reusable Bragg grating sensor was also developed where antibodies were immobilized on the optical fiber with a cleavable linkage. This allowed for the antibodies along with the captured bacteria to be removed from the optical fiber and allowed the fiber to be reloaded with new antibodies and reused[123]. These gratings have also been implemented into the self-contained optical microchip SpectroSens™, which can detect bacteria, viruses and toxins[124]–[126].

When implementing various nanocoatings, the uniformity, surface coverage, homogeneity, and intrinsic material properties of the nanostructured additions play a significant role in the sensing performance. The homogeneity and uniformity strongly influence the shape and depth of the evanescent fields, whereby if a uniform coating is not achieved, the depth of the resonance dramatically decreases, and the probing field becomes asymmetric, reducing the sensitivity[127]. Furthermore, porous coatings were seen to increase the sensor response time[106], therefore the trade-off between using nanostructured films and specific substrate materials should be thoroughly considered.

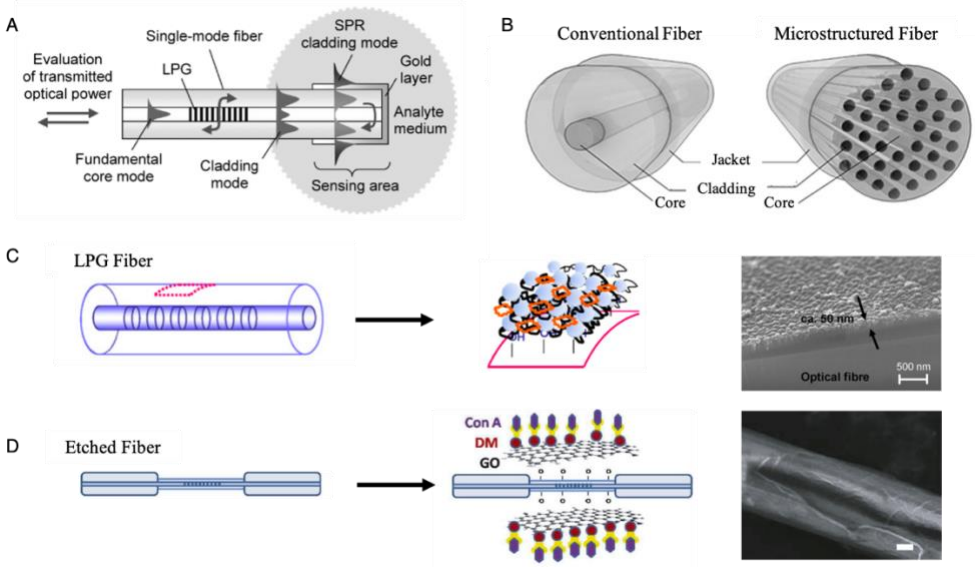

Figure 5. (A) Sensor setup employing a long period fiber grating with a gold layer generating SPR enhanced sensing. (B) Structure and main components of a conventional fiber (left) and microstructured fiber (right). (C) Deposition of a nano-assembled mesoporous coating of the polymer (poly(diallyldimethylammonium chloride)) and SiO_2 nanospheres on a fiber optic long period grating (LPG) (left). SEM image the coating cross section (right). (D) Deposition of graphene oxide on etched fiber Bragg grating, functionalized with dendrimers (DM) with specific affinity for the protein Concanavalin A (Con A) (left). SEM image of graphene oxide coating, scale bar is 2 μm (right). Reprinted with permission from (A) Schuster et al., [111] **copyright 2011 IEEE; (B) Calcerrada et al.,** [114] **copyright 2015 by WILEY-VCH Verlag GmbH & Co. KGaA, Weinheim; (C) Korposh et al.,** [118] **copyright 2012 Elsevier; (D) Sridevi et al.,** [117] **copyright 2014 Elsevier B.V.**

Overall, optical fiber gratings are a competitive refractive index-based biosensing technique as they intrinsically benefit from compactness, low weight, compatibility with optoelectronic devices, as well as being capable of multiplexing and on-site detection[127]. With the recent implementations of thin film overlays, nanocoatings and nanostructures, the sensing capabilities have broadened and allowed for enhanced sensitivities. However, there are still areas that remain relatively unexplored, such miniaturization of the optical fibers, allowing for potential implementation into areas challenging to access such as *in vivo* clinical applications[127]. Furthermore, applications have yet to fully take advantage of the ability to inscribe multiple gratings in series along a single fiber, providing compact multi-target detection. Taking this into consideration, with the abundance of enhancement

techniques developed as well as the potential areas that can still be investigated, these sensors are a promising optical platform for refractive index sensing in biological applications.

2.4 Conclusions

With the recent advancements in detecting refractive index using nanotechnology, refractive index has become a powerful tool utilized in biosensing applications. Many biological analytes have unique refractive index fingerprints, such that conducting refractive index measurements can determine the presence of analytes of interest. Functionalizing the sensor surfaces with biorecognition elements such as aptamers, antibodies and phages, allows for highly specific detection to be achieved. Furthermore, since the type of biorecognition element implemented is often not restricted by the sensing principle, the sensors can be functionalized with varying types of biorecognition components, providing versatile and multiplexed sensing abilities.

With the expansion of refractive index sensors into broad fields such as food safety, public health, and medical diagnostics, there is an incentive for optimizing detection sensitivity, specificity, cost per test and feasibility of wide scale implementation. An ideal sensor has been defined by the World Health Organization through the acronym ASSURED: Affordable, Sensitive, Specific, User-friendly, Rapid and Robust, Equipment-free and Deliverable to end-users[128]. However, not all sensor designs strive to attain every ASSURED quality. Sensing principles that allow for colourimetric detection of refractive index changes in bulk solutions provide an optical output that can be discerned with the naked eye, thus rank highly in the last four ASSURED principles. However, due to the inherent nature of the optical output, these sensing designs often are not as competitive in sensitivity and specificity. Alternatively, there is motivation to develop refractive sensors with unparalleled sensitivity and specificity for high-level sensing applications on a cellular level, rather than for bulk solutions. With these sensing techniques, there is often a trade-off on equipment-free, deliverable to end-users or being user-friendly. However, given the expansive implementation of nanostructures in refractive index sensors, as well as recent progression in portable microfluidic devices and smartphone-based technologies, it is likely that future refractive index sensors will excel in all the ASSURED qualities, providing powerful biosensing abilities capable of improving public health on a global scale.

Chapter 3
Controlling the electrostatic immobilization of gold nanoparticles onto poly(acrylic) acid

3.1 Summary

Due to the inherent sensitivity of gold nanoparticles to refractive index changes, they are commonly immobilized and used as the active component in refractive index sensing mechanisms. However, due to their ability to undergo localized surface plasmon coupling between neighbouring nanoparticles, controlling the deposition of gold nanoparticles and their degree of clustering is important to achieve the desired refractive index sensitivity. Current immobilization techniques require multiple steps, specialized equipment or access to a cleanroom. Here, a facile deposition method is provided that immobilizes gold nanoparticles onto a substrate coated with a weak polyelectrolyte via electrostatic interaction. By controlling the pH of the polyelectrolyte, as well as the size and concentration of gold nanoparticles, the degree of single and clustered nanoparticles can be regulated. This provides tunability of the optical signal strength from each nanoplasmonic population and different visual colours of the sensor surface. Furthermore, the binding strength between gold nanoparticles and the substrate was analyzed under different environmental conditions to determine limitations in which this deposition method can be applied.

3.2 Introduction

Gold nanoparticles contain unique optical and electronic properties, which make them an attractive platform for sensing applications. Resulting from their nanoscale size, gold nanoparticles exhibit LSPR, which is dependent on the particle shape, size, interparticle interactions as well as the surrounding dielectric environment. Gold nanostructures, with their inherent sensitivity to the local dielectric environment, have been implemented in a variety of refractive index sensing designs, as described in Chapter 2[16],[17],[19],[20],[28],[57]–[60]. In comparison to solution-based sensing designs, substrate-based methods offer improved reliability, repeatability, convenience as well as lower costs and, therefore, is a more attractive sensor design. However, when using deposited gold nanoparticles, the immobilization state of the nanoparticles must be considered. A variety of techniques are currently implemented to create gold nanostructured surfaces for refractive index sensing applications, including lithography, ion etching, focused ion milling, imprinting, and electron

beam deposition[16],[17],[19],[20],[28],[57]–[60]. These techniques are implemented to fabricate linearly organized arrays of gold nanostructures; however, they require at least one of the following: specialized equipment, access to a cleanroom or a series of multiple steps. Therefore, the ability to control the formation of a gold nanostructured surface with a facile and equipment-free deposition method is still a challenge.

In this Chapter, a simple tunable gold nanoparticle deposition method based on the electrostatic interaction between positively charged gold nanoparticles on a single layer of a weak negatively charged polyelectrolyte is demonstrated. It is demonstrated that by varying the pH of the polyelectrolyte layer, as well as the size and concentration of nanoparticles, the number of single and clustered nanoparticles deposited can be modulated. Due to the electrostatic nature of this deposition method, the binding efficiency of the nanoparticles is influenced by the local environment, and therefore the resilience of the electrostatic binding strength between the nanoparticles and the substrate was analyzed when exposed to various solutions and solvents.

3.3 Materials and Methods

3.3.1 Materials

Gold (III) chloride hydrate, silver nitrate, cetyltrimethylammonium bromide (CTAB), sodium borohydride, L-ascorbic acid, sodium hydroxide (NaOH), (3-aminopropyl)triethoxysilane (APTES), polyacrylic acid (PAA) (~100,000 g/mol), sodium dodecyl sulfate (SDS) as well as reagent grade ethanol, dimethyl sulfoxide (DMSO) and acetone were purchased from Millipore Sigma (Oakville, ON, Canada). Trisodium citrate dehydrate and glass coverslips were purchased from Thermo Fisher Scientific (Burlington, ON, Canada). All chemicals were used without further purification.

3.3.2 Synthesis of gold nanoparticles

Spherical gold nanoparticles were synthesized using a CTAB-mediated growth protocol using a gold nanoseed precursor[129]. To prepare the nanoseed precursor, 60 μL of newly prepared 0.1 M ice-cold sodium borohydride was added to a 20 ml solution of 2.4 x 10^{-4} M gold (III) chloride hydrate and 10^{-4} M trisodium citrate dihydrate under 1000 rpm stirring. The solution was then incubated overnight in dark ambient conditions and passed through a 0.2 μm filter before use.

To synthesize the gold nanoparticles, 3 ml of a 7.33 mM CTAB solution was added to 12 ml of Millipore water (>12 MΩcm). Under 900 rpm stirring, 0.641 ml of an 11.67 mM solution of gold (III) chloride hydrate solution was then added and allowed to stir for 1 minute. During this minute, 96

μL of a 0.5 mM $AgNO_3$ solution was added. After the 1 minute of stirring, 103 μL of a 0.1 M L-ascorbic acid was added dropwise into this solution. After the last drop was added, the appropriate volume of nanoseed was added and stirred for an additional 1.5 minutes. The amount of nanoseed determined the size of the nanoparticles synthesized and varied from 300 to 500 μL. The gold nanoparticle solution was then incubated in dark ambient conditions for 15 minutes. The solution was then centrifuged at 10 000 rpm for 15 minutes and then resuspended in a 1 mM solution of CTAB. To prepare samples for characterization, 5 μL of the solution was deposited onto a copper grid and allowed to dry overnight. The sample was then imaged using a Philips (Eindhoven, Netherlands) CM10 transmission electron microscope (TEM).

3.3.3 Immobilization of gold nanoparticles

Glass coverslips were washed by sonicating in reagent grade ethanol for 20 minutes and dried under a stream of nitrogen. The coverslips were then incubated in a solution of 2M NaOH for 20 minutes and then rinsed in Millipore water and dried under a stream of nitrogen. Following this, a 10% v/v solution of APTES was prepared in reagent grade ethanol and then immediately used to incubate the coverslips for 1 hour on a Stovall Life Science Inc. (Peosta, IA, USA) Belly Dancer orbital shaker in ambient conditions. The coverslips were then rinsed with reagent grade ethanol 3 times then dried with nitrogen. The coverslips were then immediately transferred into a polyelectrolyte solution of 20 mg/ml PAA in Millipore water for 1 hour on the orbital shaker in ambient conditions. The pH of the PAA solution was adjusted to the desired value using NaOH. The coverslips were then rinsed with Millipore water 3 times then dried with nitrogen. Before use, the gold nanoparticle solution was centrifuged at 12 000 rpm for 10 minutes and a portion of the supernatant was removed and replaced with Millipore water to achieve a CTAB concentration of 20 μM. A volume of 0.5 ml of this gold nanoparticle solution was deposited onto each coverslip, and then stored in an airtight container in dark ambient conditions overnight (around 16 hours). The following day, the remaining unbound gold nanoparticles were washed off with Millipore water and the coverslip was dried under a stream of nitrogen. The coverslips were then stored in dark ambient conditions until used.

3.3.4 Incubation in Various Solutions

An initial reading of the extinction peak was taken with the BioTek Epoch microplate spectrophotometer (Winooski, Vermont, USA) of 43 nm diameter spherical gold nanoparticles

immobilized as described in Section 3.3.3, deposited using a PAA of pH 6. Four readings were taken at different locations on each sensor surface and averaged to obtain a single representative extinction spectrum. The glass coverslips were then incubated in 3 ml of Millipore water, PBS (1%), bleach (6%), SDS (1%), or reagent grade ethanol, acetone or DMSO for a total of 60 minutes, segmented into 5 minute, 15 minute, 30 minute and 60 minute timepoints. After each consecutive timepoint, the sensor surface was removed from the solution, rinsed with 10 ml of Millipore water and dried under a stream of nitrogen. Extinction spectra were collected following the same format as the initial readings and were conducted after each incubation prior to returning the sensor into the solution for the consecutive timepoint. To determine the degree of nanoparticle loss from the sensor surface, the maximum intensity of the extinction peaks after each incubation time point was divided by the initial maximum intensity of extinction peaks from the original sensor surface. After the final 60-minute incubation, 0.5 ml of the same gold nanoparticle solution used during the initial deposition of the gold (see section 3.3.3) was deposited onto the sensor surface and stored in an airtight container in dark ambient conditions overnight (around 16 hours). The following day, the remaining unbound gold nanoparticles were washed off with 10 ml of Millipore water, dried under a stream of nitrogen and the extinction profile was collected. To determine if gold was re-deposited onto the sensor surface, the maximum intensity of the extinction peaks after the re-deposition of gold was divided by the maximum intensity of the initial extinction peaks.

3.3.5 Characterization Methods

The atomic force microscope (AFM) MFP-3D infinity (Asylum Research Company, Goleta CA, USA) with a silicon probe was used under tapping mode to image the sensor surface prior to gold nanoparticle deposition. To quantify the number of single nanoparticles and clusters deposited, the scanning electron microscope Quanta 250 FEG (Thermo Fisher Scientific, Burlington, ON, Canada) was employed under low vacuum mode to visualize the sample surface. Images were taken at 20 000 magnification to demonstrate deposition uniformity and allow for accurate determination of the types of nanoparticle clusters present.

To visualize the colourimetric response of the gold nanoparticles deposited on the coverslips, the samples were imaged using a Canon EOS Rebel T3 DSLR camera. Controlled lighting conditions were used, and the brightness and contrast of the photographs were tuned to provide the best representation of each sample. These images were then uploaded into the image processing software where RGB colour histograms were calculated. To quantify the red colourimetric shifts experienced

by the sensors, the RGB intensity of the red colour was divided by that of the summation of the blue and green intensities.

Spectrometry was used to analyze the extinction properties of the sensor surfaces and this was conducted using a BioTek Epoch microplate spectrophotometer. To compare the shape and intensities of the spectra in different conditions, the spectra were normalized to the maximum peak intensity within the relevant data set:

$$Normalized\ extinction = \frac{Measured\ extinction}{Overall\ maximum\ extinction}$$

3.4 Results and Discussion

3.4.1 Effect of polyelectrolyte deposition pH on immobilization

The synthesized gold nanoparticles were stabilized with the cationic surfactant, CTAB, which provides a positive charge on the nanoparticle surface and allows for electrostatic deposition onto a negatively charged polyelectrolyte layer (Figure 6A). The initial incubation of the base substrate is in sodium hydroxide, which deposits hydroxyls onto the substrate. This is followed by an incubation in APTES, which facilitates a silanization reaction and results in a positively charged surface. This allows for the electrostatic deposition of the negatively charged PAA, which consequently allows for the electrostatic deposition of positively charged gold nanoparticles.

It has been previously demonstrated that when layering a weak polyelectrolyte onto an oppositely charged surface, the pH of the polyelectrolyte is a contributing factor to the resulting deposited thickness[130]–[133]. This is understood with PAA through its varying degree of deprotonation. At higher pH values, PAA becomes highly deprotonated and acquires a strong negative charge, allowing it to deposit as a thin layer, with a flat chain conformation overtop a positively charged surface. However, at a lower pH value, the PAA is less ionized and acquires a weak negative charge. Therefore, when exposed to a positively charged substrate, a thicker layer containing open loop-rich coils of PAA would settle onto the substrate surface to balance the positive charges on the underlying substrate. In the protocol used for the deposition of gold nanoparticles onto the PAA functionalized surface, the deposited layer of the PAA is exposed to the gold nanoparticle solution which has a neutral pH around 6.5 to 7. The pK_a of PAA is inherently 4.2, however when it is exposed to the gold nanoparticle solution, apparent pK_a is lowered to around 3 or 4[134]. Due to the reduced apparent pK_a, all conformations of the PAA layers become highly ionized with comparable charge densities when exposed to the gold nanoparticle solution. In this environment, the

ionized PAA layers contain varying amounts of total charge depending on the thickness of the deposited layer. The different amounts of charge overcompensation created by the thickness of the PAA layers are the source of the various deposition profiles of the gold nanoparticles. Since deposition at the lower pH values create thicker layers of PAA, these samples have more overall charge, allowing for the deposition of more gold nanoparticles. Furthermore, due to the extended physical conformation of the PAA caused by the low deposition pH, the surface is also more prone to nanoparticle clusters depositing (Figure 6B). In comparison, at higher pH, depositions with a smoother PAA conformation and less overall negative charge, fewer nanoparticles deposit and less clusters form. The conformational changes of the underlying PAA with depositions at pH values ranging from 2 to 8 were observed using AFM (Figure 7). In accordance with the larger degree of single nanoparticles deposited on a higher pH PAA, the extinction spectrum for these surfaces showed a dominant extinction peak in the low 500 nm range, confirming their presence (Figure 8A). This was further confirmed with the SEM images of the substrate samples showing primarily single nanoparticles and small clusters in pH 6 and 8 samples (Figure 8C). Whereas with decreasing pH, a more dominant extinction peak appeared in the mid 700 nm range on the extinction spectrum, representing the increase in cluster deposition (Figure 8A). This was confirmed with the increase in prevalence of large clusters in the SEM images (Figure 8C). The different extinction spectra with the various deposition profiles also created unique colours of the gold nanoparticle surfaces, ranging from dark blue to a red-orange (Figure 8B).

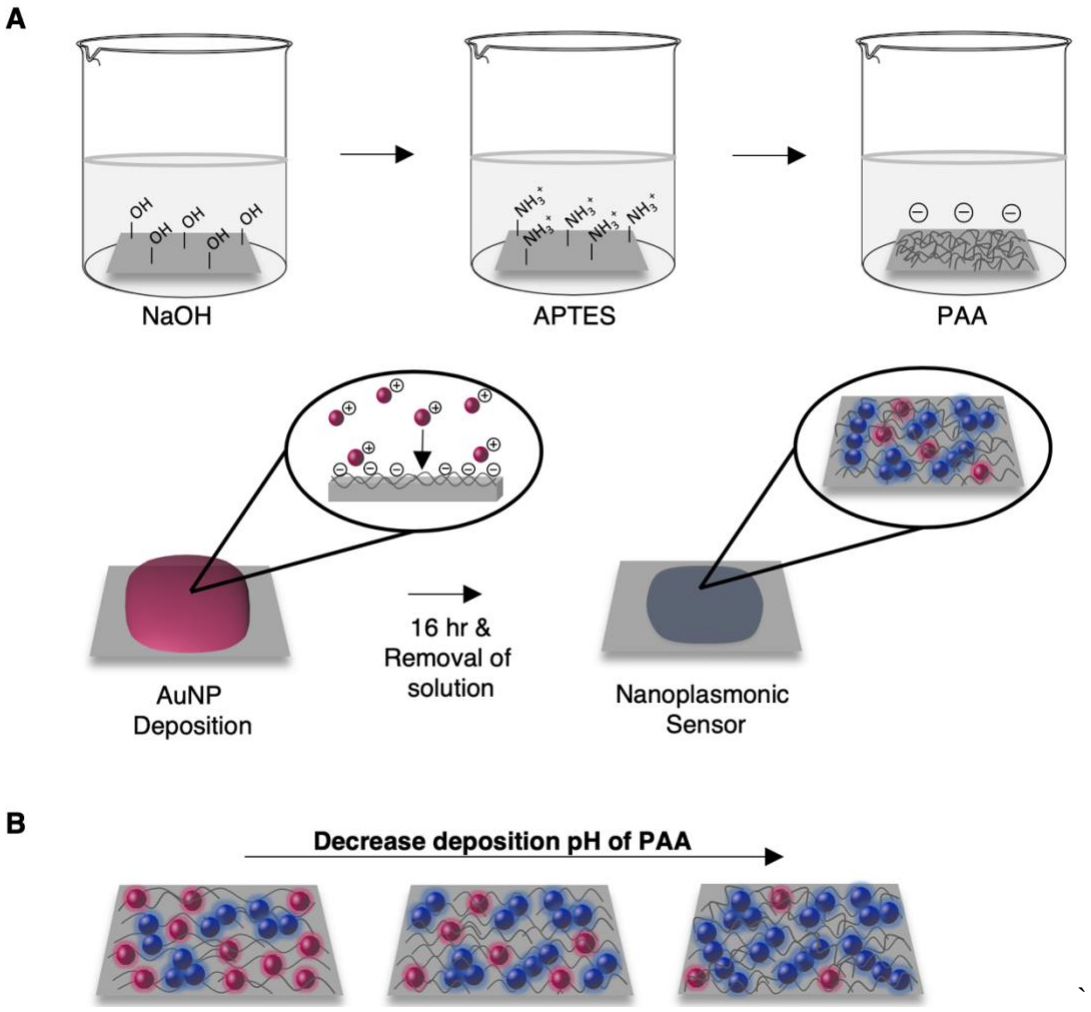

Figure 6. A) Schematic of the surface functionalization steps used to electrostatically deposit gold nanoparticles onto the PAA. B) Schematic of the relationship between the pH of the PAA and the deposition characteristics of the gold nanoparticles.

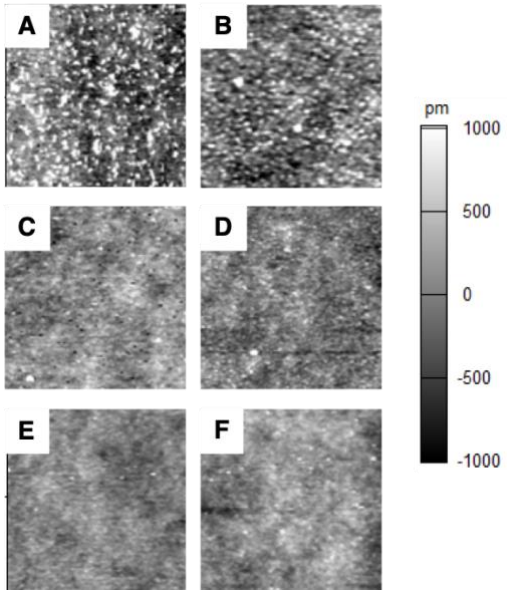

Figure 7. Atomic force microscopy topographic images of glass substrates with surface modifications of (A) PAA pH 2 (B) PAA pH 4 (C) PAA pH 6 (D) PAA pH 8 (E) Sodium hydroxide treatment and (F) APTES monolayer formation. All images are 2.0 µm x 2.0 µm.

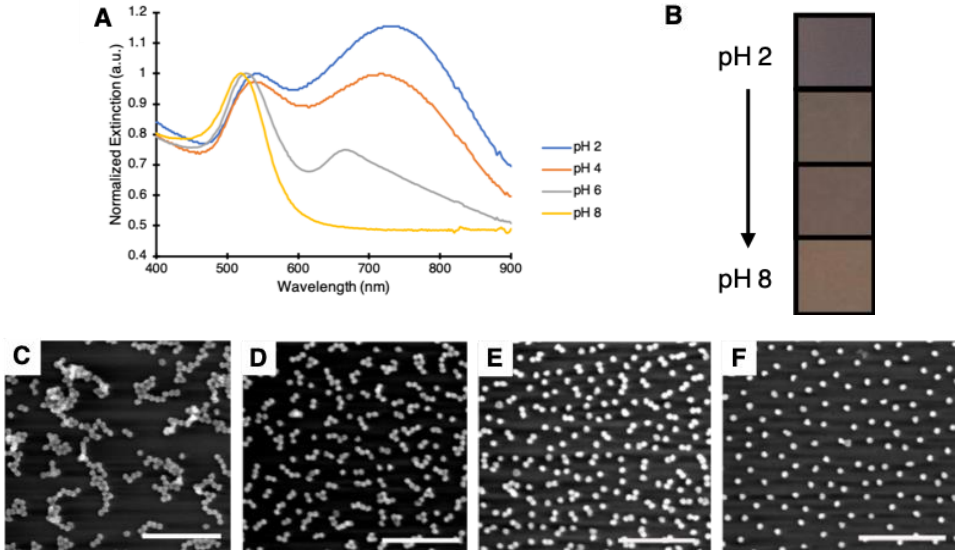

Figure 8. A) Peak normalized extinction spectra of gold nanoparticle surfaces with varying PAA pH depositions. Gold nanoparticles have a diameter of 44.1 nm ± 2.7nm (mean ± standard

deviation). B) Photographs of gold nanoparticle sensor surfaces displaying different visual colours for varying PAA pH depositions. C-F) SEM images of gold nanoparticles deposited on PAA with a pH of 2, 4, 6, and 8 respectively.

3.4.2 Effect of size and concentration of gold nanoparticle on immobilization

By varying the concentration of the gold solution used in the deposition step, the degree of single and clustered nanoparticles deposited can be modulated. By reducing the concentration of gold nanoparticles deposited onto the functionalized coverslip, fewer clusters deposit on the sensor surface, however, this also coincided with fewer total nanoparticles, resulting in weaker extinction spectra (Figure 9A,B,C). With a significantly lower number of gold nanoparticles deposited, a smaller active surface area was present on the surface. This lead to a less intense colour, which is not ideal when observing visual colourimetric signals (Figure 9A,B,C). To combat this reduction in total active surface area on the sensor, while still maintaining a low cluster to single nanoparticle ratio, dilute concentrations of larger gold nanoparticles were deposited (Figure 10A,B,C). The larger nanoparticles provide a greater active surface area per nanoparticle and created a prominent visual colour on the sensor surface even with the reduced number of total nanoparticles. Consequently, the ratio of single nanoparticles to clusters could be tailored without losing the intensity of the visual colour of the sensor. For example, sensors containing gold nanoparticles with an average diameter of 83 nm and concentration of 22 nanoparticles per μm^2 experienced an active gold surface on 11.9% of the sensor and were bright pink in colour. Conversely, sensors containing gold nanoparticles with an average diameter of 22 nm and concentration of 158 nanoparticles per μm^2 experienced active gold surface on only 6.0% of the sensor surface and appeared a very faint yellow colour. Therefore, by depositing larger gold nanoparticles, lower concentrations of nanoparticles could be deposited while maintaining a sufficient active surface area for a discernable visual response.

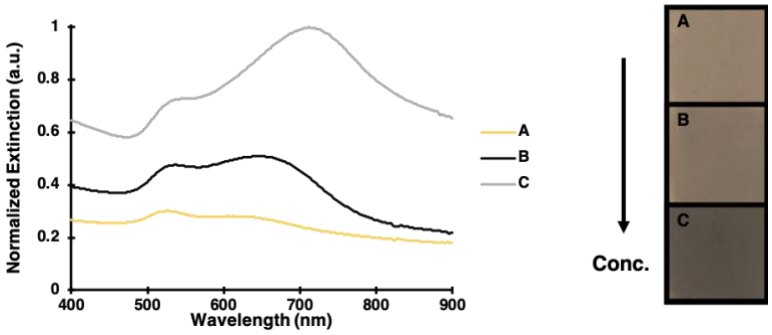

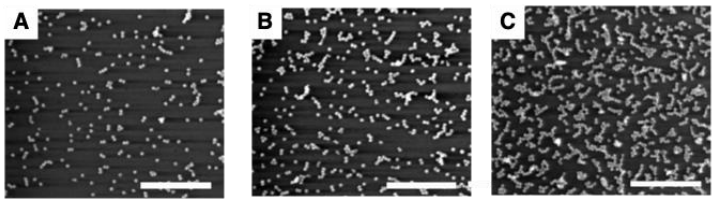

Figure 9. Peak normalized extinction spectra, photographs and SEM images of 22 nm diameter gold nanoparticle surfaces with varying gold nanoparticle concentrations. A) 158 nanoparticles/μm$_2$ B) 272 nanoparticles/μm$_2$ C) 563 nanoparticles/μm$_2$.

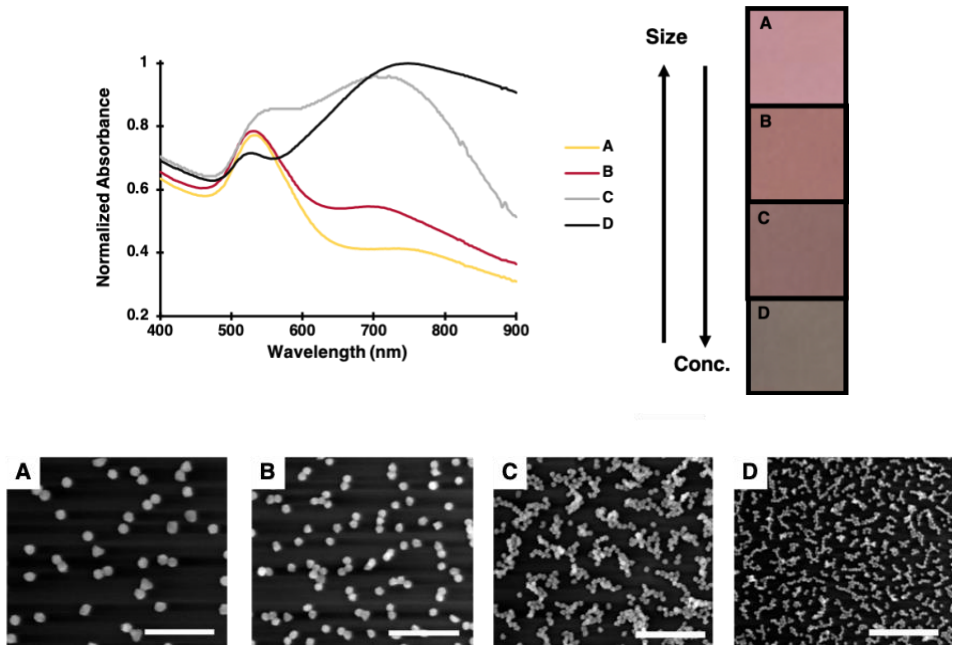

Figure 10. Peak normalized extinction spectra, photographs and SEM images gold nanoparticle surfaces with varying gold nanoparticle size and concentrations. A) 83 nm diameter and 22 nanoparticles/μm$_2$ B) 57 nm diameter and 45 nanoparticles/μm$_2$ C) 42 nm diameter and 150 nanoparticles/μm$_2$ D) 22 nm diameter and 563 nanoparticles/μm$_2$. Scale bar: 500nm.

3.4.3 Environmental Compatibility of Gold Nanoparticle Deposition

Due to the electrostatic nature of the attachment method of the gold nanoparticles, the strength of the nanoparticle-PAA interactions is subject to change when exposed to different solvents or solutions due to their screening effects. Furthermore, since the underlying layer of PAA is also attracted to the substrate via electrostatic attraction, the strength of the PAA attachment is also

vulnerable to screening by external solvents or solutions. To analyze how the sensor surface reacts under various conditions, the gold coated glass slides were incubated in various solutions. To determine if gold nanoparticles were removed from the substrate during the incubation, the extinction intensity of the sensor was read before and after each incubation and the intensity of the extinction peaks were compared (Figure 11). An extinction peak with lower intensity would correspond to lost gold nanoparticles on the sensor surface, either from a loss of nanoparticles, or a loss of PAA which in turn, resulted in a loss of nanoparticles. To specify if only gold was removed or if PAA was also removed from the substrate, after exposure to the test solution, the surfaces were then incubated overnight with a gold nanoparticle solution, identical to the one used in the initial deposition step. After the removal of the remaining non-bound gold nanoparticles the following day, the new extinction profile of the sensor surface was examined. If the extinction peaks of the surface regained the initial intensities, it was concluded that the test solution removed the gold nanoparticles and the PAA remained bound, since new nanoparticles were still electrostatically attracted to the sensor surface. However, if the extinction peaks did not regain the full initial intensity, it was determined that the test solution removed the PAA along with the nanoparticles, which would hinder the re-deposition of the new gold nanoparticles.

The sensor surfaces were tested in various washing or cleaning solutions including 1% SDS (a surfactant commonly found in cleaning and hygiene products), 0.6% bleach, 6% H_2O_2, Millipore water, and reagent grade acetone, ethanol and DMSO. These solutions are either polar or ionic in nature, therefore providing screening effects between the positively charged gold nanoparticles and the negatively charged PAA. After the 60 minutes of total incubation time, the percent of the extinction intensity remaining for both the primary and secondary peaks are given in Table 1.

Table 1. Percent remaining of the maximum extinction intensity of the primary and secondary peaks after a 60 minute incubation period in various solutions and solvents.

	% of Primary Peak Remaining, (Standard Deviation)	% of Secondary Peak Remaining, (Standard Deviations)
Ethanol	90.6, (0.4)	90.5, (2.7)
Acetone	93.9, (3.9)	89.0, (5.4)
DMSO	85.6, (1.6)	79.6, (2.2)

Bleach	87.4, (1.3)	76.1, (1.4)
Millipore	94.7, (1.7)	95.7, (2.7)
PBS	83.8, (2.2)	85.2, (1.5)
H_2O_2	91.9, (3.2)	94.7, (2.7)
SDS	84.7, (2.4)	85.7, (1.7)

Since all solutions resulted in some loss of gold nanoparticles, this restricts the sensor surface to be functional in predominantly dry environments. As seen in the sensors exposed to PBS, ethanol, acetone, SDS, DMSO and bleach, a significant loss of nanoparticles was experienced after 5 minutes of exposure, thus confirming that even short exposures to these solutions should be minimized to maintain functionality. Furthermore, with the exception of the surfaces incubated in DMSO, the gold nanoparticles were effectively redeposited and achieved an average extinction profile intensity within 5% of its initial value (Figure 12). Therefore, the lowered extinction intensities seen in Figure 11, with the exception of the sample incubated in DMSO, can be attributed to a loss of gold nanoparticles, without a significant loss of the underlying PAA. In the case of DMSO, the re-deposited secondary peak reached an extinction peak 14.8% lower than the initial secondary peak. However, this trend was not seen in the primary peak which regained 99.99% of its initial intensity. This result is likely caused by an induced change in the surface conformation of the PAA, rather than the loss of the PAA. Since a linear and smooth surface conformation of PAA was previously confirmed to promote the deposition of single nanoparticles and hinder the deposition of clustered nanoparticles, it is probable that the DMSO stimulated a structural change of the PAA, resulting in a smoother surface, which would explain the full recovery of single nanoparticles and a substantial loss of clustered nanoparticles.

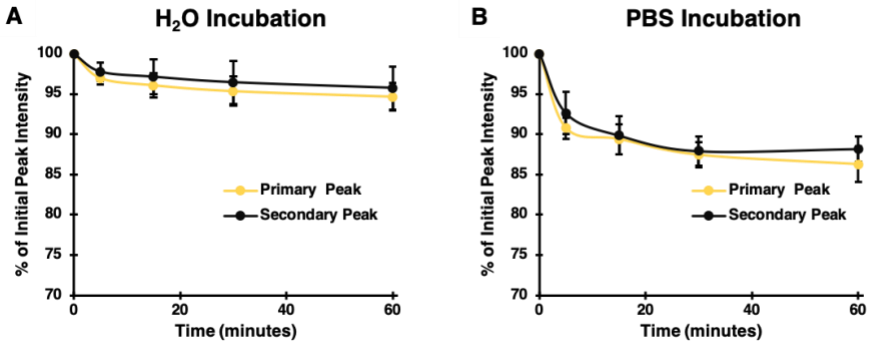

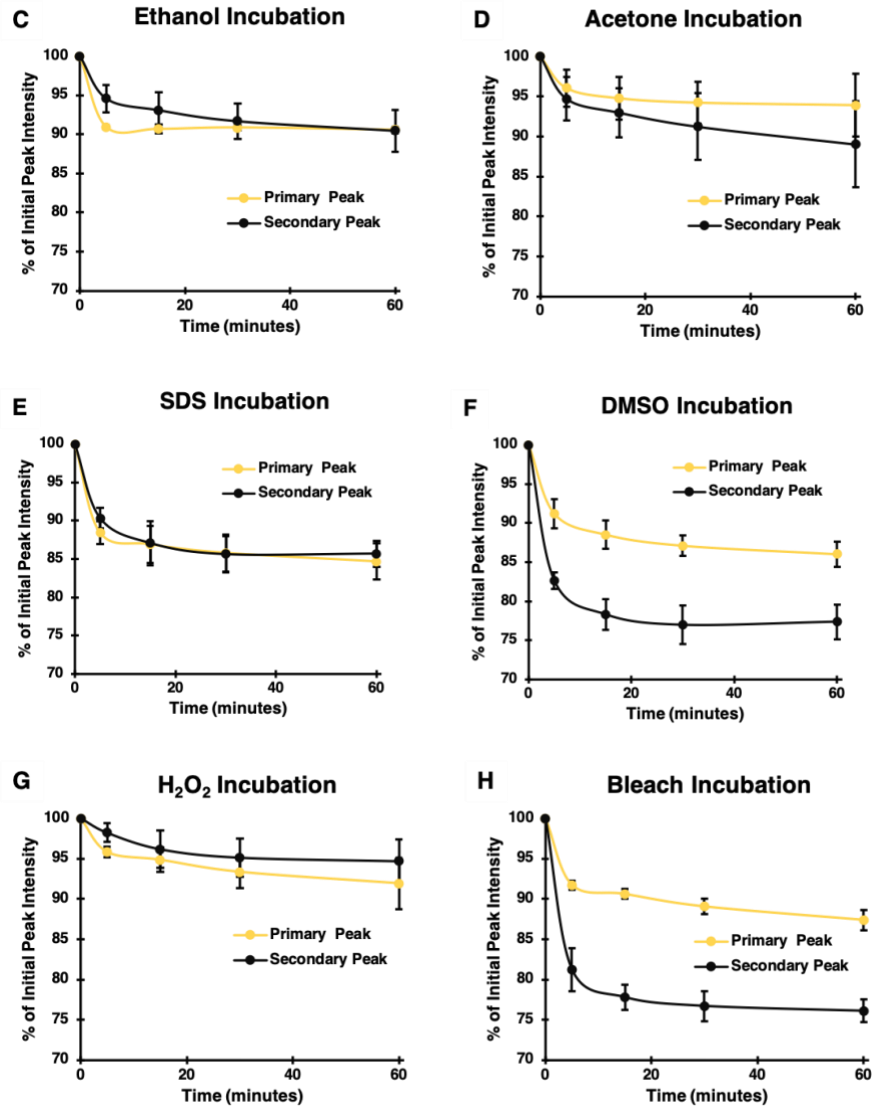

Figure 11. Primary and Secondary extinction peak intensity over various incubation times in A) Millipore water B) 1% PBS C) Ethanol D) Acetone E) 1% SDS F) DMSO G) 6% H2O2 H) 0.6% Bleach

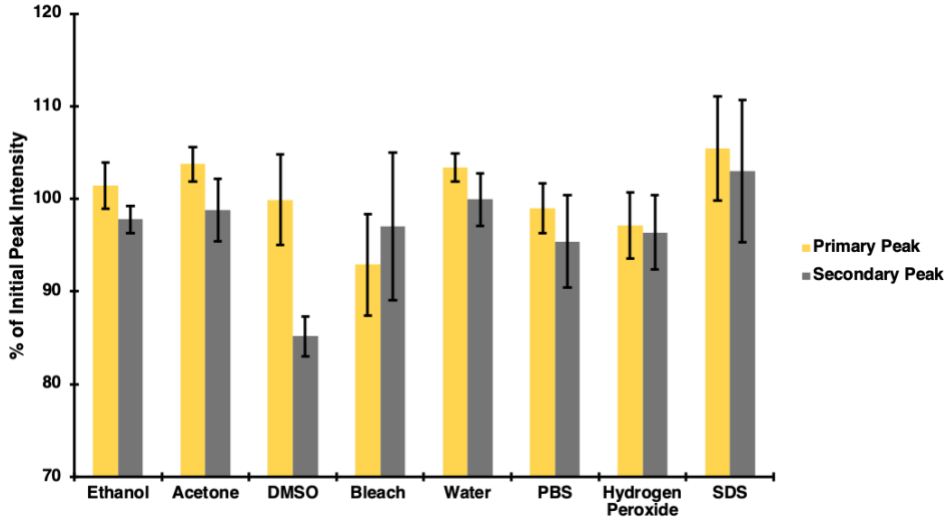

Figure 12. Redeposition efficiency of gold nanoparticles on sensor surfaces after incubation in various solutions and solvents.

3.5 Conclusions

The ability to deposit gold nanoparticles onto a glass surface allowing for the degree of single nanoparticles and clustered nanoparticles deposited to be individually tuned was demonstrated. This immobilization technique utilized the electrostatic attraction between the weak negatively charged polyelectrolyte, PAA, and the positively charged gold nanoparticles. The ratio of single nanoparticles to clustered nanoparticles immobilized could be modulated by adjusting the pH of the PAA layer as well as the concentration of the gold nanoparticle solution used for deposition. Furthermore, the optical signal strength could be maintained at low nanoparticle concentrations with the use of larger gold nanoparticles, such that a visual colour could be observed over a range of gold nanoparticle concentrations. Due to the electrostatic nature of the gold nanoparticle deposition, exposure of the nanoplasmonic surface to polar or ionic solutions resulted in a screening effect which hindered the electrostatic interactions between the nanoparticles and the substrates. This resulted in a loss of nanoparticles from the substrate surface and highlighted the incompatibility of the sensor surface with common cleaning solutions and solvents. These results act as a guide to outline the restrictions of the sensor for commercial implementation.

Chapter 4
Colourimetric refractive index detection

4.1 Summary

The refractive index of a material describes the how light propagates through the medium and is defined as the speed of light in a vacuum divided by the phase velocity of light in the medium. Refractive index sensors are commonly employed in a range of fields due to the broad scope of information that can be deduced from a refractive index measurement. The determination of the refractive index of a material provides information on the degree to which light is refracted or reflected when interacting with the material, and can determine the temperature, pressure and level of stress the material is experiencing. Furthermore, changes in refractive index can indicate the presence of analytes, which has been frequently exploited in biosensing applications to detect analytes ranging from bacteria to cancer cells. With the versatility that refractive index measurements offer, refractive index sensors have been incorporated into applications in the fields of optics, photonics, biomedicine and materials science. With this large demand and growing need for user-friendly refractive index sensors that provide rapid and robust detection, the nanoplasmonic surface described in Chapter 3 was implemented as a colourimetric refractive index sensor. Depending on the deposition profile of the gold nanoparticles deposited on the surface, a blue to red or a red to blue colour shift can be achieved in response to an increase in refractive index, allowing for a customizable colour sensing profile. Furthermore, it was demonstrated that the sensor surface could be re-used multiple times, thus increasing its desirability for implementation into commercial products.

4.2 Introduction

The inherent refractive index sensitivity of gold nanoparticles is imparted by their free electrons, which are resonantly excited by light to generate LSPR oscillations. The resonant frequencies of these LSPR oscillations are dependent on the local refractive index and therefore, shifts in the oscillation wavelengths provide a means to determine shifts in refractive index. The relationship between the resonant wavelengths of the LSPR and the local refractive index can be modelled through the Mie theory estimation in the long-wavelength, electrostatic dipole limit for spherical metallic nanoparticles, through the equation[135],[136]:

$$E(\lambda) = \frac{24\,\pi N_A\, a^3\, \varepsilon_m^{\frac{3}{2}}}{\lambda \ln(10)} \left[\frac{\varepsilon_i}{(\varepsilon_r + \chi\varepsilon_m)^2 + \varepsilon_i^2} \right] \qquad \text{Equation 1}$$

Where $E(\lambda)$ is the extinction, N_A is the density, a is the radius of the nanoparticle, ε_m is the dielectric constant of the environment, λ is the wavelength of the absorbing radiation, ε_i and ε_r are the imaginary and real portion of the nanoparticle's dielectric function and χ describes the shape of the nanoparticle (2 for a sphere). The surface plasmon resonance peak that is responsible for the colour of the nanoparticle is generated when ε_r equals $-2\varepsilon_m$, which corresponds to an enhancement of the electromagnetic field[135], [136]. For gold nanoparticles, this is satisfied in the visible region of the spectrum, therefore allowing them to be used as visual detecting agents in sensing applications.

In this chapter, the simple, tunable and equipment-free gold nanoparticle deposition method discussed in Chapter 3 is employed as a ratiometric refractive index sensor, which can provide a red to blue as well as a unique blue to red colourimetric shift. The ratiometric design of this nanoplasmonic sensor incorporates single nanoparticles and clustered gold nanoparticles, corresponding to extinction peaks around 530 nm and 700 nm respectively. The two populations of nanoparticles produce competing optical signals, where the single nanoparticles emit a red visual colour and the clustered nanoparticles emit a blue visual colour. The initial colour of the sensor surface depends on the ratio of each population of gold present on the surface. However, a colour shift observable by the naked eye is experienced with a change in refractive index, as the local dielectric environment modulates the ratio of absorption intensity of the single and clustered gold nanoparticles. This ratiometric shift in the optical intensities provides the foundation for the unique ratiometric optical signal observable by the naked eye.

4.3 Materials and Methods

4.3.1 Materials

All the chemicals and containers used in this study were purchased from the same sources as those mentioned in Chapter 3 unless otherwise stated. In addition, Glycerol was purchased from Millipore Sigma (Oakville, ON, Canada).

4.3.2 Synthesis of gold nanoparticles

Spherical gold nanoparticles were synthesized from the procedure using CTAB-mediated growth from a gold nanoseed precursor described in Chapter 3[129]. Briefly, to prepare the nanoseed precursor, 60 μL of newly prepared 0.1 M of ice-cold sodium borohydride was added to a 20 ml solution of 2.4 x 10^{-4} M gold (III) chloride hydrate and 10^{-4} M trisodium citrate dihydrate under 1000 rpm stirring. The solution was then incubated overnight in dark ambient conditions and passed through a 0.2 μm filter before use.

To synthesize the gold nanoparticles, 3 ml of a 7.33 mM CTAB solution was added to 12 ml of Millipore water (>12 MΩcm). Under 900 rpm stirring, 0.641 ml of an 11.67 mM solution of gold (III) chloride hydrate solution was then added and allowed to stir for 1 minute. During this minute, 96 μL of a 0.5 mM $AgNO_3$ solution was added. After 1 minute of stirring, 103 μL of a 0.1 M L-ascorbic acid was added dropwise into this solution. After the last drop was added, the appropriate volume of nanoseed was added and stirred for an additional 1.5 minutes. The gold nanoparticle solution was then incubated in dark ambient conditions for 15 minutes. The solution was then centrifuged at 10 000 rpm for 15 minutes and then resuspended in a 1 mM solution of CTAB.

4.3.3 Immobilization of gold nanoparticles

Gold nanoparticles were electrostatically immobilized onto glass surfaces using the protocol developed in Chapter 3, using a PAA layer deposited at pH 4. Briefly, glass coverslips were washed by sonicating in reagent grade ethanol for 20 minutes and dried under a stream of nitrogen. The coverslips were then incubated in a solution of 2M NaOH for 20 minutes and then rinsed in Millipore water and dried under a stream of nitrogen. Following this, a 10% v/v solution of APTES was prepared in reagent grade ethanol and then immediately used to incubate the coverslips for 1 hour on the belly dancer orbital shaker in ambient conditions. The coverslips were then rinsed with reagent grade ethanol 3 times then dried with nitrogen. The coverslips were then immediately transferred into a polyelectrolyte solution of 20 mg/ml PAA in Millipore water for 1 hour on the orbital shaker in ambient conditions. The pH of the PAA solution was adjusted to pH 4 using NaOH. The coverslips were then rinsed with Millipore water 3 times then dried with nitrogen. Before use, the gold nanoparticle solution was centrifuged at 12 000 rpm for 10 minutes and a portion of the supernatant was removed and replaced with Millipore water to achieve a CTAB concentration of 20 μL. A volume of 0.5 ml of this gold nanoparticle solution was deposited onto each coverslip, and then stored in an airtight container in dark ambient conditions overnight (around 16 hours). The following day,

the remaining unbound gold nanoparticles were washed off with Millipore water and the coverslip was dried under a stream of nitrogen. The coverslips were then stored in dark ambient conditions until used.

4.3.4 Ultraviolet-visible spectroscopy

Aqueous solutions of glycerol were prepared with refractive index values of 1.37, 1.41, 1.44 and 1.47. An aliquot of 30 μL of Millipore water was first deposited onto the gold nanoparticle surface and the extinction profile was read, using the Epoch microplate spectrophotometer, where the nanoparticles were exposed to the Millipore water. The gold nanoparticle surface was dried under a stream of nitrogen and 30 μL of the glycerol solution with a refractive index of 1.37 was then deposited on the nanoparticle surface. The extinction profile of the surface exposed to the glycerol solution was then collected. The surface was then washed with 10 ml of Millipore water to remove the glycerol solution and then dried under a stream of nitrogen. This deposition, analysis and washing steps were repeated for the glycerol solutions, with refractive index values of 1.41, 1.44 and 1.47. The extinction spectra were read, from a range of 400 nm to 900 nm with a step size of 2 nm.

4.4 Results and Discussion

4.4.1 Optical response of gold nanoparticles to refractive index

A determining factor of the LSPR experienced by gold nanoparticles is the restoring force of the oscillating electrons, which determines their oscillation frequency and consequently, the wavelengths of light that couple to the nanoparticles. When gold nanoparticles are exposed to an increase in refractive index, as explained using Mie theory equation 1, longer wavelengths of light couple to the oscillating conduction electrons of the nanoparticles. This shift is caused by the increase in dielectric function, which accompanies higher refractive index solutions and correlates to an increase in electronic polarizability of the solution. Highly polar mediums are better able to attenuate surface charges and therefore, the oscillating conduction electrons from the gold nanoparticles exposed to higher refractive index solutions experience a dampened restoring force. With a smaller restoring force, the resonance frequency of these electrons is shifted to lower energies and couple to light with longer wavelengths. This red-shift in LSPR produces a blue-shift in the observed colour of the gold nanoparticles and has been utilized in colourimetric refractive index sensors designed, using arrays of isolated nanoparticles or nanostructures[16],[17],[19],[20],[28],[57]–[60].

With the incorporation of two populations of gold nanoparticles, a novel optical response to an increase in refractive index was experienced by the nanoplasmonic surface, providing a visual red-shift rather than the standard blue-shift in the observed colour. Depositing both single and clustered nanoparticles onto a substrate created two extinction peaks, one at high energy blue-green wavelengths (565 nm, corresponding to the isolated nanoparticles) and one at low energy red wavelengths (726 nm, corresponding to clustered nanoparticles). As demonstrated in Chapter 3, the high energy extinction peak, or primary peak contributed to a red or orange visual colour, whereas the low energy extinction peak, or the secondary peak contributed to a blue colour. When the sensor surface was exposed to an increased refractive index, these two extinction peaks experienced different optical responses, extending beyond the red peak shift caused by the dampened restoring force. Both peaks demonstrated a red wavelength shift and an increase in extinction intensity, however, the intensity increase experienced by the primary peak was more significant than that experienced by the secondary peak. This difference in intensity between the primary and secondary peaks created a stronger visual colourimetric signal than that from the red-shift experienced by both the peaks, and therefore, resulted in an overall blue to red colourimetric shift.

This ratiometric trend was demonstrated in sensor surfaces with different concentrations of single and clustered nanoparticles as well as different sized gold nanoparticles (Figure 13). This provides the foundation for the visual ratiometric property of the refractive index sensor creating a colourimetric shift.

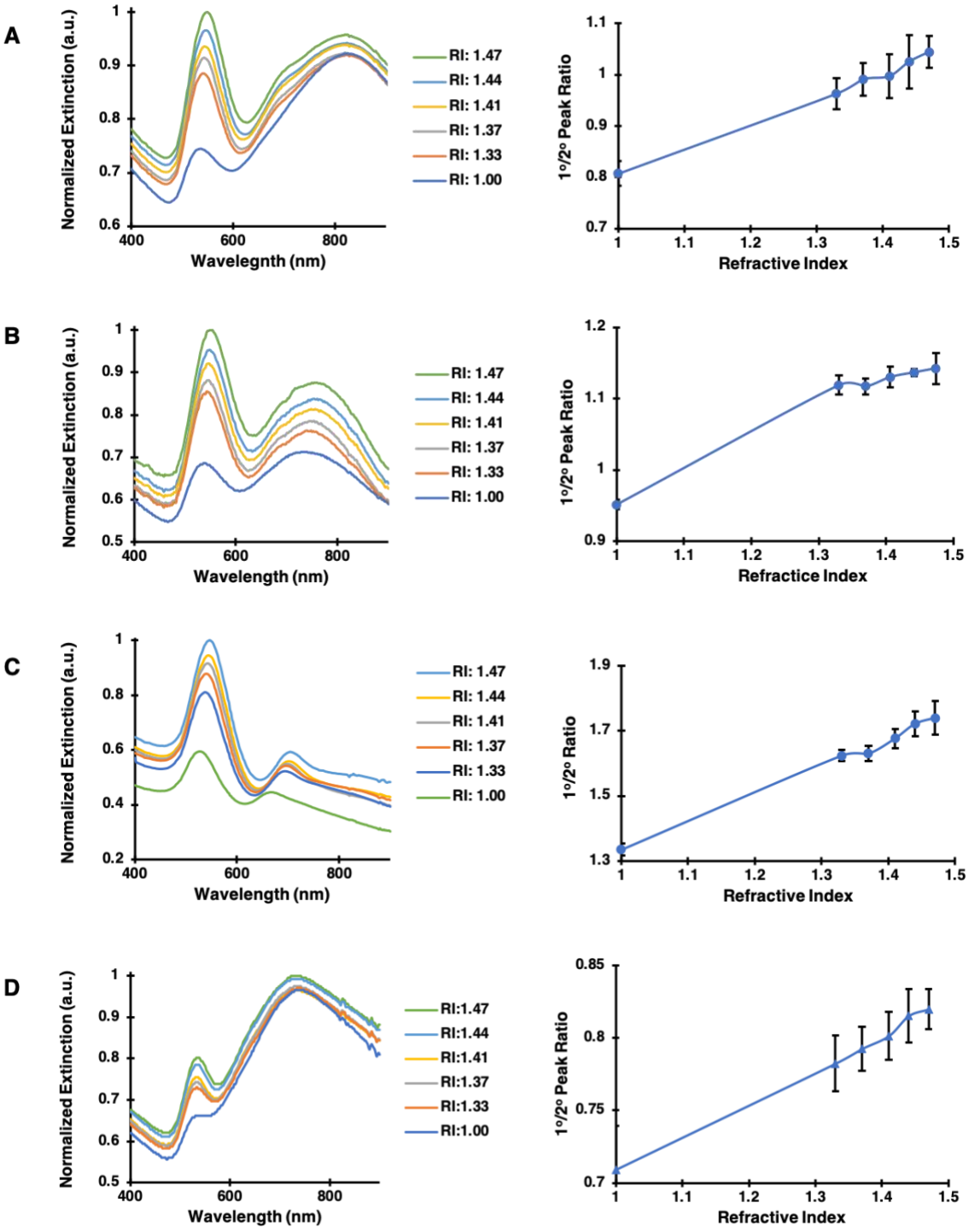
A
Normalized Extinction (a.u.)
Wavelegnth (nm)
RI: 1.47
RI: 1.44
RI: 1.41
RI: 1.37
RI: 1.33
RI: 1.00
1°/2° Peak Ratio
Refractive Index
B
Normalized Extinction (a.u.)
Wavelength (nm)
RI: 1.47
RI: 1.44
RI: 1.41
RI: 1.37
RI: 1.33
RI: 1.00
1°/2° Peak Ratio
Refractice Index
C
Normalized Extinction (a.u.)
Wavelength (nm)
RI: 1.47
RI: 1.44
RI: 1.41
RI: 1.37
RI: 1.33
RI: 1.00
1°/2° Ratio
Refractive Index
D
Normalized Extinction (a.u.)
Wavelength (nm)
RI:1.47
RI:1.44
RI:1.41
RI:1.37
RI:1.33
RI:1.00
1°/2° Peak Ratio
Refractive Index

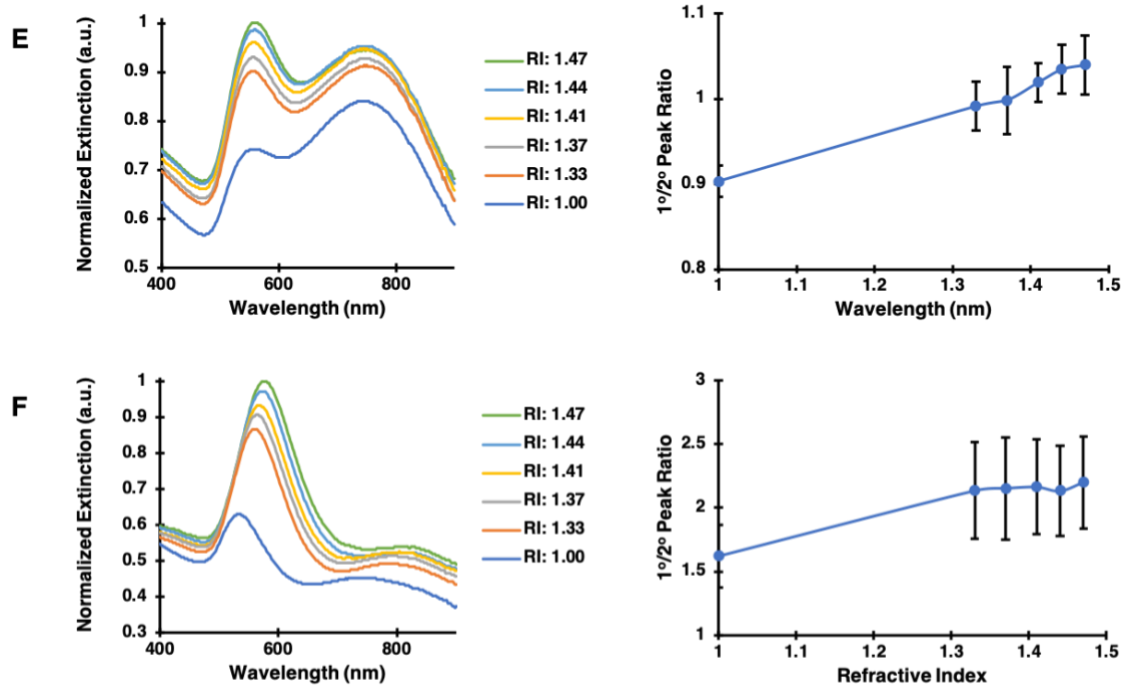

Figure 13. Peak normalized UV-Vis extinction spectra showing ratiometric response to refractive index values of 1.00 (air), 1.33 (Millipore water), 1.37, 1.41, 1.44 and 1.47 (glycerol solutions). (A-C) Sensors deposited with gold nanoparticle diameters 43 nm and A) PAA pH 2, B) PAA pH 4 C) PAA pH 6. Error bars denote standard deviation of readings on different locations on the sensor surface (N=3). (D-F) Sensors deposited with PAA pH4 and gold nanoparticles with diameters and concentrations of D) 22 nm, 563 NP/μm$_2$ E) 40 nm, 279 NP/μm$_2$ and F) 83 nm, 22 NP/μm$_2$. Error bars denote standard deviation of readings on different sensor surfaces (N=3).

As the extinction profile dictates the visual colour of the sensor surface, this ratiometric response created a set of unique colour shifts with the different nanoplasmonic surfaces. As mentioned earlier, the primary peak contributed a red or orange visual colour whereas the secondary peak contributed a blue visual colour. With the combined presence of both these populations, the observed colour is a blend of the two colour outputs. However, with the increase in local refractive index stimulating the increase in the primary extinction peak intensity, the red visual colour gained strength and a red colourimetric shift was observed, opposite of the traditional blue colour shift experienced from the reduced LSPR restoring force. However, this red-shift was only visible when there was a sufficient balance between the two extinction peaks. With a dominant primary peak and

only a subtle secondary peak, the primary peak largely governs the initial colour of the sensor surface (Figure 14 A). Consequently, the red optical output consistently dominates over the blue optical output and the ratiometric functionality of the surface is removed. Consequently, when exposed to an increase in refractive index, a visual blue-shift will be observed, similar to that experienced by the deposition of a homogenous single gold nanoparticle population. Alternatively, with a large secondary peak and a weak primary peak, the blue colour from the secondary peak dominates the colour of the surface. If the imbalance between the extinction peaks is sufficiently large, even with the increase in primary peak intensity when exposed to the higher refractive index, the ratiometric shift may not be substantial enough to create a visual colour shift (Figure 14 G). Therefore, in order to achieve a discernable red colourimetric shift from the sensor surface, the initial ratio of single to clustered nanoparticles is optimized when the extinction peaks achieve roughly similar intensities, such that both colours are initially represented, and the increase in the red colourimetric output with refractive index is not overpowered by the initial blue colourimetric output (Figure 14 B-F). A summary of the colourimetric shifts for various refractive index environments have been collected for sensor surfaces deposited with varying PAA pH values as well as for varying gold nanoparticle sizes and concentrations (Figure 14). The RGB colour profile was also determined for each image, and the red-shift was quantified by calculating the Red/(Blue+Green) values (Figure 15). An overall trend of increasing red shift was generally seen, except for the sensor represented in Figure 14A and 15A, which was dominated by single nanoparticles and experienced the blue colourimetric shift classically seen for homogenous gold nanoparticles.

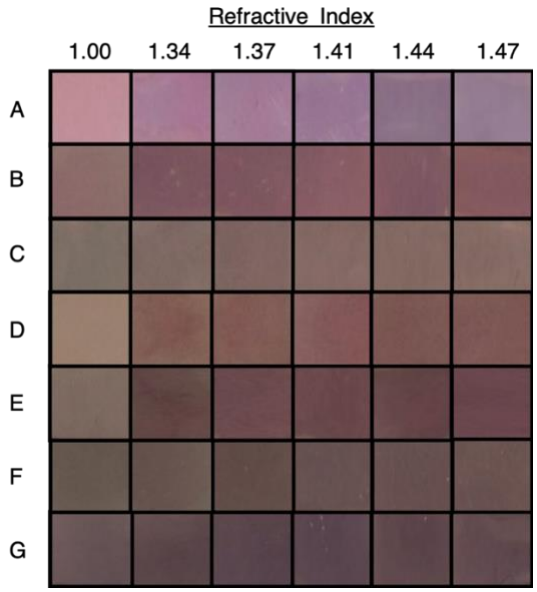

Figure 14. Photographs of representative areas of the sensor surface exposed to refractive index values of 1.00 (air), 1.34, 1.37, 1.41, 1.44 and 1.47 using various concentrations of aqueous glycerol solutions. (A-C) Sensors deposited with PAA pH 4 and gold nanoparticles with diameters A) 83 nm B) 40 nm and C) 22 nm. (D-G) Sensors deposited with gold nanoparticle diameters 43 nm and D) PAA pH 8 E) PAA pH 6 F) PAA pH 4 G) PAA pH 2.

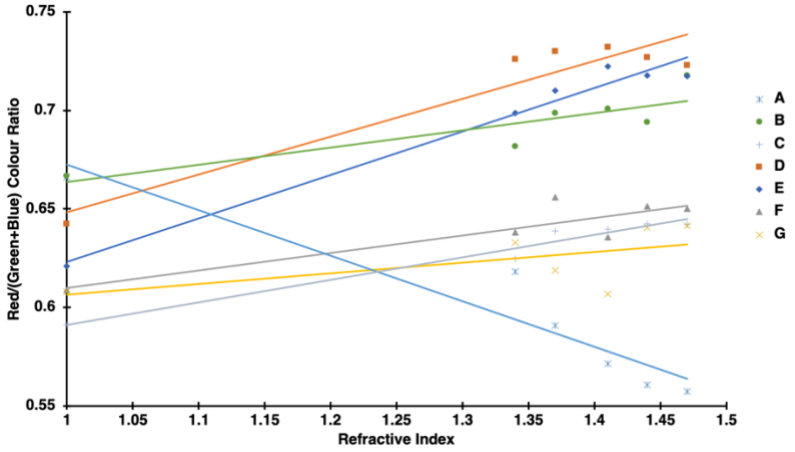

Figure 15. Red colourimetric shift using RGB ratio (Red/[Green+Blue]) experienced by the sensor surfaces when exposed to increasing refractive index. (A-C) Sensors deposited with PAA pH 4 and gold nanoparticles with diameters A) 83 nm B) 40 nm and C) 22. (D-G) Sensors deposited with gold nanoparticle diameters 43 nm and D) PAA pH 8 E) PAA pH 6 F) PAA pH 4 G) PAA pH 2.

As observed in the ratiometric response profiles of the various sensor surfaces (Figure 13), the nanoplasmonic surfaces containing smaller gold nanoparticles experienced weaker increases in the primary peak extinction intensity in response to refractive index changes than the sensors composed of larger gold nanoparticles. Similarly, the primary extinction peaks from the smaller gold nanoparticles also experienced a smaller red-shift in primary peak intensity. These results suggest that the smaller gold nanoparticles have a weaker refractive index sensitivity than larger gold nanoparticles, which is consistent with previously published literature[137]. This finding can further be explained by the degree of coverage the gold nanoparticles experience from the underlying PAA layer. As explained in Section 3.4.1, the gold nanoparticles are electrostatically attracted to the PAA layer, and part of the active surface area of the gold nanoparticles is exposed to the PAA layer and consequently shielded from the external environment. With a constant PAA pH, the height of the PAA should be consistent, however, the percent of the nanoparticle surface area exposed to the external environment would vary based on the size of the nanoparticle. For comparison, a small nanoparticle would experience a greater relative degree of PAA shielding from the external environment than a larger nanoparticle, and thus would be less sensitive to changes in refractive index in the external environment. For confirmation of the differing responses to refractive index changes corresponding to the gold nanoparticles sizes, the expected optical response of single gold nanoparticles was simulated. The extinction cross section σ_{ext} was calculated from the formulas:

$$\sigma_{\text{ext}} = \frac{2\pi}{k^2}\sum_{j=1}^{\infty}(2j+1)\text{Re}\left(a_j + b_j\right) \qquad \text{Equation 2}$$

$$a_j = \frac{m\,\psi_j(\omega)\,\psi_j'(v) - \psi_j(v)\,\psi_j'(\omega)}{m\,\psi_j(\omega)\,\xi_j'(v) - \xi_j(v)\,\psi_j'(\omega)} \qquad \text{Equation 3}$$

$$b_j = \frac{\psi_j(\omega)\,\psi_j'(v) - m\,\psi_j(v)\,\psi_j'(\omega)}{\psi_j(\omega)\,\xi_j'(v) - m\,\xi_j(v)\,\psi_j'(\omega)} \qquad \text{Equation 4}$$

$$\psi_j(x) = \sqrt{\frac{\pi x}{2}}\,J_{j+\frac{1}{2}}(x) \qquad \text{Equation 5}$$

$$\xi_j(x) = \sqrt{\frac{\pi x}{2}}\left[J_{j+\frac{1}{2}}(x) + i\,Y_{j+\frac{1}{2}}(x)\right] \qquad \text{Equation 6}$$

These equations were used to simulate the extinction cross section a spherical nanoparticle with a radius of r_0 and complex permittivity of $\varepsilon = n^2$ exposed to a plane wave with an angular frequency of $\frac{2\pi c}{\lambda_0} = kc/n_m$ where $m = n/n_m$, $v = kr_0$, $\omega = mv$ and embedded in a dielectric medium with an electric permittivity of $\varepsilon_m = n_m^2$. Simulations were executed with spherical gold nanoparticles with diameters of 22 nm, 40 nm and 83 nm, which mimic the size of the experimental gold nanoparticles. Refractive index sensitivities were compared based on the red-shift of the primary extinction peak from the exposure of air to Millipore water. However, to effectively compare the red-shifts caused by refractive index changes calculated theoretically and observed experimentally, the effective refractive index experienced by the gold nanoparticles must be fully considered. In the sensor design, the gold nanoparticles were deposited on a layer of PAA, and consequently, experienced a local refractive index that combined both the index of the PAA as well as the external environment. It has been established that the effective refractive index, n_{eff}, experienced by a gold nanoparticle, partially enclosed by substrate is calculated using the following equation

$$n_{eff} = (1 - \alpha)n_{sub} + \alpha n_{med}$$

where n_{sub} is the refractive index of the substrate, n_{med} is the refractive index of the medium and α is the section of the particle's surface area immersed in the medium[138]. For a single isolated nanoparticle, with diameters of 22 nm, 40 nm and 83 nm, the PAA coverages are estimated to be 93.64%, 88.44% and 42.62% respectively. Therefore, the effective refractive index values when exposed to air and to Millipore water are 1.468 and 1.489 for 22 nm nanoparticles, 1.4422 and 1.4803 for 40 nm nanoparticles as well as 1.213 and 1.402 for 83 nm nanoparticles. Simulated red shifts from these refractive index transitions were 2nm, 4nm and 30 nm for 22 nm, 40 nm and 83 nm gold nanoparticles (Figure 16). This was relatively consistent with the experimental red shifts experienced which were 2.7 nm $\pm$ 1.5 nm, 7 nm $\pm$ 2.6 nm. and 27.7 nm $\pm$ 2.1 nm for 22 nm, 40 nm and 83 nm gold nanoparticles (Figure 16).

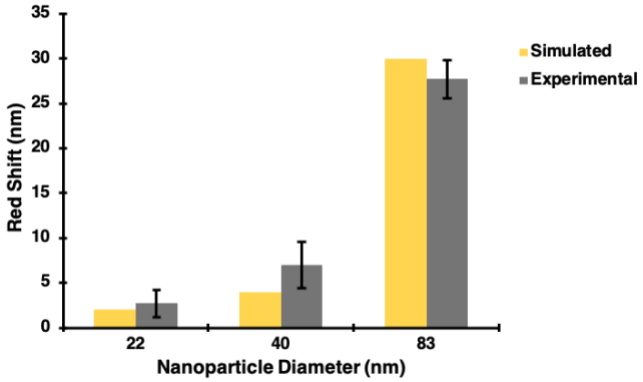

Figure 16. Simulated and experimental red shifts under the external environment shift of 1.00 to 1.33 with the effective refractive index values of 1.468 and 1.489 (22 nm diameter), 1.4422 and 1.4803 for (40 nm diameter) as well as 1.213 and 1.402 for (83 nm diameter). Note: the experimental red shift error bars denote the standard deviation (N=3).

When comparing experimental results to simulated calculations, it is necessary to note inconsistencies between the simulated design and the physical design of the prototype sensor. Experimentally, the single nanoparticles were deposited on surfaces in proximity to neighbouring nanoparticles whereas the simulation assumed an isolated nanoparticle. As mentioned previously, the immobilized gold nanoparticles on the sensor surface experience localized surface plasmon oscillations, stimulated by incident light, which are confined to the nanoparticle surface and known as near-fields. When nanoparticles are within the near proximity to other nanoparticles, the near-field of nanoparticles can be felt by neighbouring nanoparticles and near-field coupling occurs[139], [140]. Consequently, the electric field that each particle experienced in the experimental setup would be composed of the incident light field as well as the near-field of neighbouring nanoparticles. Near-field interactions result in lower energy coupled plasmon oscillations and a red-shift of the LSPR wavelength. The relationship between the red-shift in the peak wavelength and the interparticle distance has previously been established through the following equation[141]:

$$\Delta\lambda/\lambda_o = \frac{14.3\mathcal{E}_m(1+\gamma)^2}{(12\Lambda\left(\frac{s}{D}+1\right)^3-(1+\gamma))(464.6+14.3\mathcal{E}_m\gamma)} \qquad \text{Equation 7}$$

Where $\Delta\lambda/\lambda_o$ is the shift in wavelength normalized by the incident wavelength, $\mathcal{E}_m$ is the medium dielectric constant, γ is a constant that depends on the shape of the nanoparticle, (2 for spheres), *D* is the particle dimension parallel to the axis of the nanoparticle coupling (equal to the

diameter for spheres), *s* is the interparticle distance and *Λ* is based on the other particle dimensions (1 for spheres). From this equation, it is demonstrated that near field coupling increases with decreasing interparticle distance and increasing nanoparticle size[142],[141]. As the $\Delta\lambda/\lambda_o$ increases with increasing refractive index, the $\Delta\lambda/\lambda_o$ was calculated for each size of gold nanoparticle when exposed to the highest experimental refractive index, 1.47, to determine if the coupling would have a significant effect on the optical output. On average, the interparticle distances for the nanoplasmonic surfaces with the 22 nm, 40 nm and 83 nm gold nanoparticles were 23.2 nm, 30.4 nm and 75.2 nm respectively. However, the 1/*e* values of the $\Delta\lambda/\lambda_o$ (above which, coupling is deemed significant) are at interparticle distances of 7 nm, 12.75 nm, and 26.5 nm for the sensors with 22 nm, 40 nm and 83 nm nanoparticle diameters respectively (Figure 17). Since the experimentally determined interparticle distances are larger than these values, it can be concluded that the interparticle coupling between the nanoparticles immobilized on the sensor surfaces does not largely contribute to the optical properties of the sensor surface.

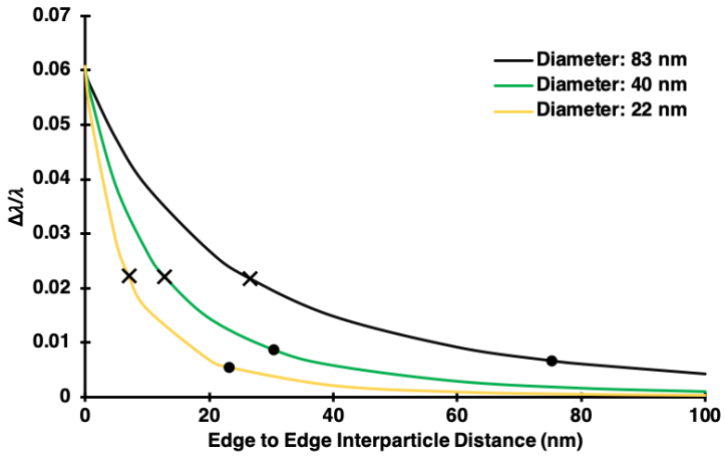

Figure 17. Strength of near-field interactions plotted as a function of interparticle distance, denoted as the change in resonant wavelength divided by the resonant wavelength of an isolated nanoparticle. Calculated for gold nanoparticles with diameters of 22 nm, 40 nm and 83 nm and effective refractive indices of 1.498, 1.497 and 1.483 respectively. X markers indicate the 1/*e* values and circle markers indicate the average values experienced experimentally.

Another important difference between the experimental setup and the simulation assumption is that experimentally, the gold nanoparticles immobilized by PAA are deposited onto a glass substrate whereas the simulation is conducted as though the nanoparticles are surrounded by a homogeneous medium. To make the assumption that these systems experience similar optical

responses to their local surroundings, it is important to understand how the glass substrate affects the optical properties of the deposited nanoparticles. Since the substrate used to deposit the gold nanoparticles is a dielectric material, it does not experience inherent plasmon resonances. Consequently, the surface does not interact directly with the plasmon resonance of the deposited particles nor generate surface-hybridized plasmon modes. However, the substrate does provide a screening effect on the electromagnetic fields responsible for the restoring force on the gold nanoparticles' plasmon oscillations[143]. This screening effect reduces the symmetry around the nanoparticle, such that the electromagnetic fields from a nanoparticle close to a dielectric surface differs from that of a nanoparticle surrounded by a homogeneous environment. The strength of the screening produced from the dielectric substrate is equivalent to the potential generated by a nanoparticle image with its image charges reduced by a factor of $(\varepsilon - 1)/(\varepsilon + 1)$ where ε is the permittivity of the substrate[143],[144]. Dielectric substrates with larger permittivity create stronger nanoparticle "images" and thus, experience larger interactions with the deposited gold nanoparticles. These interactions result in plasmon resonance red-shifts where the degree of red-shift is based on the nanoparticle-substrate distance, the substrate permittivity as well as the polarization of the incident light. A shorter nanoparticle-substrate separation, higher substrate permittivity and incident light polarized perpendicular to the substrate result in a larger nanoparticle-substrate screening interaction and therefore, create a larger red-shift in the plasmon resonance of the deposited nanoparticle[145]. It was previously determined that a vacuum approximation of the behaviour of a nanoparticle can be used when the nanoparticle is supported on a low-index substrate and using incident light parallel to the substrate[143]. It was also seen on glass substrates, which have a low-index (n=1.52), that there was a relatively small difference between the spectra of gold nanoparticles with incident light polarized perpendicular and parallel to the substrate, and the difference only manifested itself strongly in substrates with higher permittivity[143]. For these reasons, along with the PAA preventing the direct contact between the gold nanoparticles and the glass surface, it is approximated that the glass substrate did not create a significant effect on the gold nanoparticles.

4.4.2 Repeatability

For commercial use of this gold nanoparticle-based refractive index sensor, it is desirable for the sensor surface to be re-used multiple times. Consequently, repeatability tests were conducted on various sensor surfaces to show the ability for the sensor to return to its original ratiometric state after the deposition and removal of various refractive index solutions (Figure 19). It was observed that

regardless of the initial ratio of deposited single and clustered gold nanoparticles or the underlying pH value of the PAA layer, the extinction peaks from the gold nanoparticles were efficient at returning to their initial intensities. The small degree of gold nanoparticle loss that was experienced was likely due to the mechanical force exerted on the surface during the washing step to remove the glycerol solutions. Glycerol has a moderately high viscosity of 1.412 Pascal seconds, and since the shear stress exerted on the surface by a fluid is proportional to the viscosity, when the glycerol solutions are washed from the surface, they exert relatively strong shear stress on the gold nanoparticles, which is probably the main contributing factor to the nanoparticle loss.

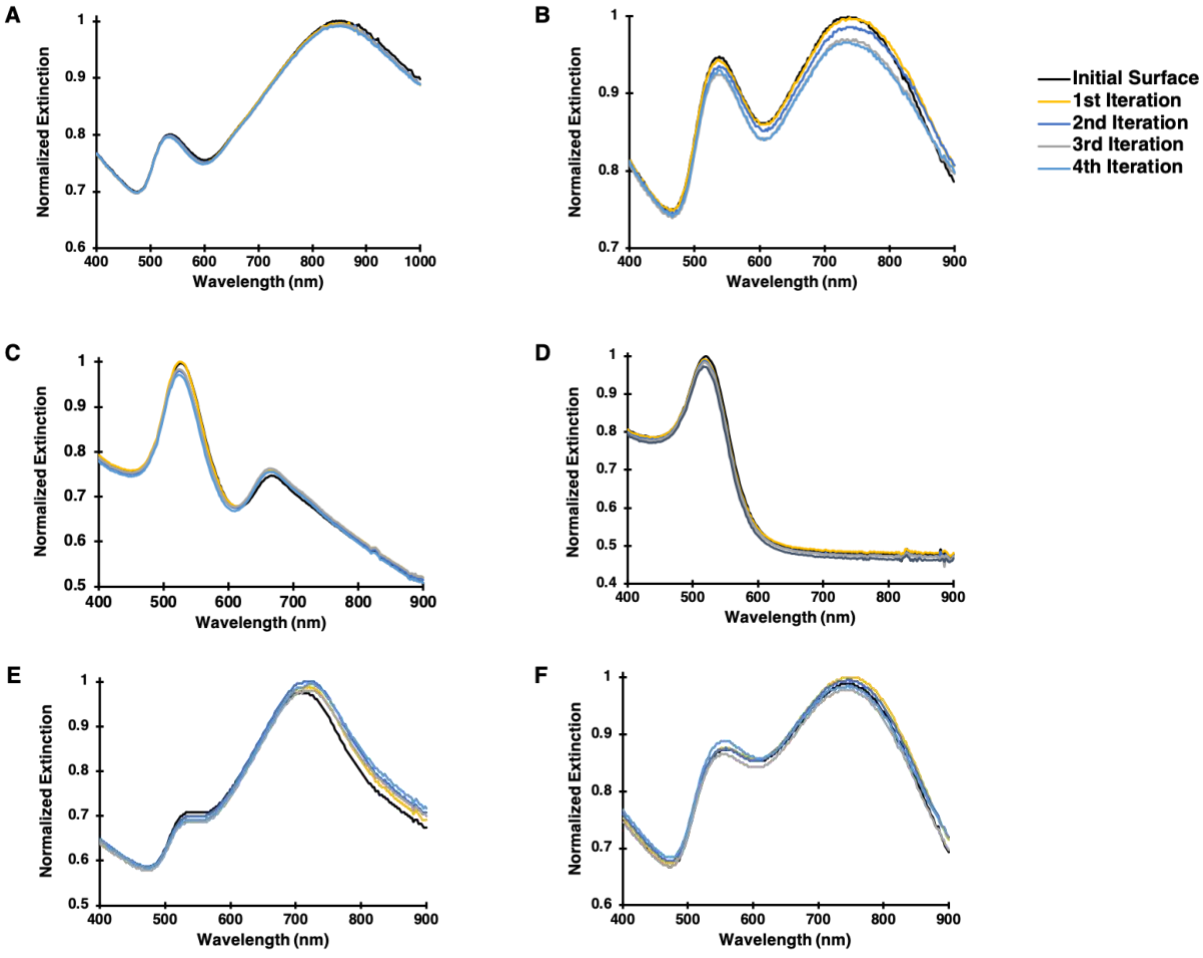

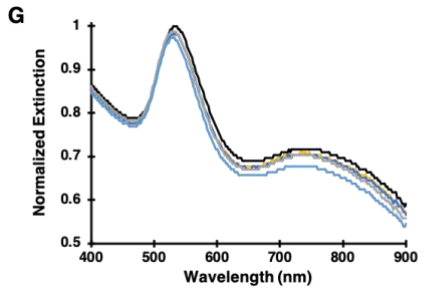

Figure 18. Reusability of sensor surface, shown through restoration of initial extinction spectra after deposition and removal of refractive index solutions. (A-D) Sensors deposited with gold nanoparticle diameters 43 nm and A) PAA pH 2 B) PAA pH 4 and C) PAA pH 6. D) PAA pH 8 (E-G) Sensors deposited with PAA pH 4 and gold nanoparticles with diameters E) 22 nm F) 40 nm and G) 83 nm. Iteration 1: refractive index 1.33, Iteration 2: refractive index 1.37, Iteration 3: refractive index 1.41, Iteration 4: refractive index 1.44.

4.5 Conclusion

A novel nanoplasmonic surface using immobilized gold nanoparticles was implemented as a refractive index sensor with a proven detection range of 1.00 to 1.47. Based on the gold nanoparticle deposition profile, a red to blue as well as a unique blue to red colourimetric shift has been achieved. The colour changes were dependant on the initial ratio of the immobilized single and clustered nanoparticles and were produced by the ratiometric optical response experienced by the two populations. It was demonstrated that the colour change could be interpreted by the naked eye and thus, allow for easy user adaptation. For those with difficulties visually identifying colours, the colour change could be quantified through simple image analysis techniques and a smartphone application can be developed in the future for easy interpretation of the results. In addition, the sensor surfaces were shown to be reusable after the deposition and removal of various refractive index solutions, improving its cost efficiency and ability to be implemented as a commercially viable sensor.

Chapter 5
COMSOL Simulations Study

5.1 Summary

The ratiometric response achieved in Chapter 4 using various ensembles of gold nanoparticles provides a new avenue for ratiometric refractive index sensing. Nanoplasmonic sensor designs implemented for ratiometric refractive index sensing have currently been limited to theoretical simulations of specialized nanoparticle architectures and have yet to be demonstrated experimentally or theoretically with simplistic gold nanospheres[19], [20]. So far, a prototype for a ratiometric refractive index sensor by depositing ensembles of gold nanospheres was developed, however, extending beyond this experimental demonstration and analyzing how the unique response is achieved would greatly enhance the impact of this research. Here, each nanoparticle ensemble was individually simulated, allowing the contribution of each nanoparticle component on the sensor surface to be analyzed. This provides a mechanistic understanding of how the refractive index induced ratiometric response achieved.

5.2 Introduction

To date, there has not been a nanoplasmonic-based ratiometric refractive index sensor observed in the literature similar to the sensor described in Chapter 4. Therefore, developing a mechanistic understanding of the sensor properties involved in this novel ratiometric response would create a valuable contribution to existing scientific literature surrounding the use of gold nanoparticles in refractive index sensing. It has been previously demonstrated in the literature that LSPR coupling increases the refractive index sensitivity of the component nanoparticles[146], [147]. However, in the sensor developed in Chapter 4, the optical shift observed for the coupled LSPR extinction peak was weaker than that of the uncoupled LSPR peak, which is an unexpected finding. The reasoning for this unique observation lies in the unique positioning of the gold nanoparticle clusters and will be analyzed in this Chapter.

Simulations of the constituent nanoparticle ensembles observed experimentally were compiled to achieve a theoretical ratiometric response similar to the experimental response, thereby elucidating a mechanistic understanding as to how the ratiometric response occurs. By simulating each component nanoparticle cluster separately, the contributions of the individual ensembles could

be isolated and analyzed. Since the nanoparticle clusters were stochastically deposited with nanometer variances in interparticle distances and variations in PAA surface coverage, each cluster type was represented through multiple models to produce an optical response accounting for the inherent variations. The result of the stochastic deposition was that clusters with identical shapes experienced a wide range of interparticle LSPR coupling, and thus, varying secondary extinction peaks. On the contrary, the uncoupled LSPR was not largely affected by the stochastic deposition and thus, the primary extinction peaks remained relatively consistent between models with a single cluster shape. Similarly, the secondary extinction peaks experienced greater variances than the primary extinction peaks when comparing extinction profiles of clusters with different shapes. Consequently, when combining the simulated models to create a representation of the overall sensor surface, the intensity of the primary peaks had a larger overlap and was more additive than the intensity of the secondary peaks. Therefore, when exposed to an increase in refractive index, the primary extinction peak experienced a concentrated intensity increase, whereas the intensity increase experienced by the secondary extinction peak was diluted over a broader wavelength range. This resulted in the intensity change to be more pronounced in the primary peaks compared to the secondary peaks, creating a ratiometric response similar to that experienced experimentally.

5.3 Methods of Simulation

The extinction cross section of the nanoplasmonic surface was numerically calculated using the commercially available COMSOL Multiphysics 5.4 with the built-in Wave Optics Module. The simulation was composed of three sections, the gold nanoparticle or gold nanoparticle cluster, an embedding medium and a perfectly matched layer. The gold nanoparticle clusters were oriented in the y and z plane and the calculations were taken with electric fields polarized along both the y and z directions in the perfectly matched layer. The perfectly matched layer was used to prevent reflection effects at the simulation boundaries. The space was discretized with a fine meshing algorithm and the extinction cross section, σ_{ext}, (Equation 10) was calculated by summing the scattering cross section, σ_{sc}, (Equation 8) and the absorbance cross section, σ_{abs} (Equation 9).

$$\sigma_{sc} = \frac{1}{I_0} \iint (n \cdot S_{sc})\, dS \qquad \text{Equation 8}$$

$$\sigma_{abs} = \frac{1}{I_0} \iiint Q\, dV \qquad \text{Equation 9}$$

$$\sigma_{ext} = \sigma_{sc} + \sigma_{abs}$$ Equation 10

In Equation 8, *n* is a normal vector pointing away from the nanoparticle, S_{sc} is the scattered intensity vector and I_0 is the incident intensity with the integral calculated over the surface area of the scattering nanoparticles. In Equation 9, *Q* is the power loss density of the nanoparticles and the integral is calculated over the nanoparticle volume. The σ_{abs} and σ_{sc} values calculated for electric fields polarized along the y and z directions were averaged together and summed for a final σ_{ext} value. The wavelength range that the simulations were conducted over was 390 nm to 760 nm in increments of 10 nm and the calculations used the real and imaginary part of the dielectric constant for gold previously determined in the literature[148]. The simulations used gold nanoparticles with a radius of 20 nm and cluster sizes and orientations were based on the experimentally determined ensembles present on a pH 6 deposition of PAA.

5.4 Results and Discussion

To theoretically confirm the ratiometric profile experimentally observed on the nanoplasmonic surfaces, simulations were conducted with nanoparticle arrangements and local environments specified to match the experimental values. As mentioned in Chapter 4.4.1, the gold nanoparticles experienced an effective refractive index, n_{eff}, that combined both the refractive index of the PAA as well as the refractive index of the external environment. The influence on the n_{eff} from the PAA and the local environment depend on the proportion that the gold nanoparticles are surrounded by each medium, which is determined by the thickness of the PAA layer as well as the gold nanoparticle size. As determined in Chapter 3.4.1, the conformation of the deposited PAA layer depended on its pH, where higher pH values favour the deposition of thin layers and lower pH values result in thick layers. By matching the experimentally determined primary extinction peak locations with the simulated primary extinction peak locations, it was found that with the PAA deposited at pH 6 and gold nanoparticles 40 nm in diameter, the nanoparticles experienced a n_{eff} that corresponded to approximately 56% of the surface area covered by the PAA and 44% of the surface area exposed to the external environment. However, since the PAA coverage of the gold nanoparticles and clusters is not strictly controlled, it is likely that the various nanoparticles and nanoclusters experience a range of PAA coverage. Therefore, the simulations were conducted for PAA coverage of 46%, 56% and 66% and given weightings of 0.25, 0.5 and 0.25 respectively, which provided effective refractive index values of 1.23, 1.28 and 1.33 (Figure 19). With these effective refractive index values, the primary

peak locations ranged from 522 nm to 528 nm with a standard deviation of 3 nm, and the secondary peak locations ranged from 598 nm to 620 nm with a standard deviation of 11 nm. It can therefore be concluded that the change in effective refractive index creates a larger variation in the secondary peak location than the primary peak location. The significant shift in secondary extinction peak is a result of the changing degree of interparticle coupling experienced with changing refractive index. As noted from Equation 7, a higher refractive index environment allows for increased interparticle coupling, thus resulting in progressively red shifted extinction peaks.

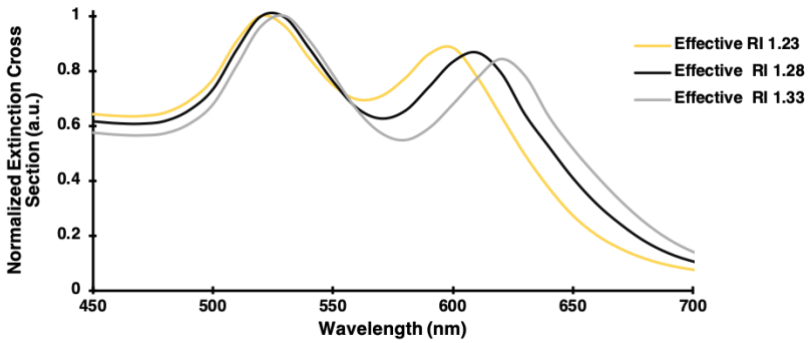

Figure 19. Simulated normalized extinction cross section of gold nanoparticles with interparticle spacings of 0 nm, 1 nm and 2 nm weighted at 0.25, 0.5 and 0.25 respectively. Shown for effective refractive index values of 1.23, 1.28 and 1.33 corresponding to PAA coverages of 46%, 56% and 66% respectively and exposed to an external environment with a refractive index of 1.00.

In addition to conducting simulations using realistic effective refractive index values, the different nanocluster arrangements as well as their prevalence must be taken in consideration as they strongly influence the extinction spectrum experienced by the nanoplasmonic surface (Figure 20). The frequencies of the various gold nanoparticle cluster types were determined by counting their occurrence in representative SEM images, totaling an area of 6.5 μm^2. Based on the different nanoparticle orientations, the primary peaks observed in the single nanoparticles as well as the clustered nanoparticles were relatively consistent ranging from 525 nm to 538 nm, with a standard deviation of 4.49 nm (Table 2). Conversely, the secondary peaks observed in the different cluster shapes experienced larger variations in the peak location ranging from 611 nm to 680 nm, with a

standard deviation of 27.72 nm (Table 2). Thus, when combined together, they create a broader secondary peak compared to the primary peak and do not stack as efficiently.

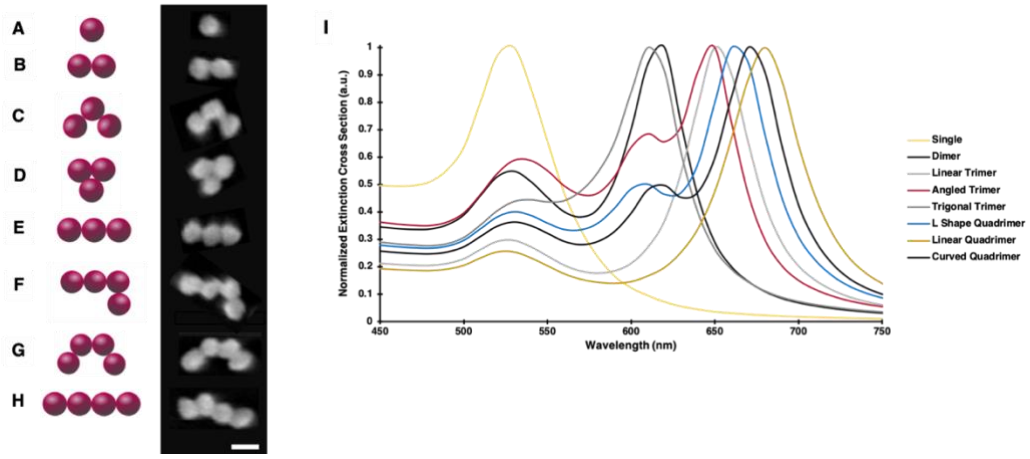

Figure 20. (A-H) SEM images along with model representations of cluster shapes simulated. Scale bar 50 nm. A) Single B) Dimer C) Angled Trimer D) Trigonal Trimer E) Linear Trimer F) L Shape Quadrimer G) Curved Quadrimer H) Linear Quadrimer I) Simulated normalized extinction cross sections of gold nanoparticle ensembles from (A-H) exposed to a refractive index of 1.33 with interparticle spacing 0 nm.

Table 2 Primary and secondary peak locations of the nanoparticle ensembles deposited on the sensor surface with percent prevalence.

Nanocluster Shape	Primary Peak Location (nm)	Secondary Peak Location; Sub Secondary Peak Location (if applicable) (nm)	Prevalence in PAA pH 6 (%)
Single	527	-	57.45
Dimer	529	618	34.11
Linear Trimer	526	651	2.87
Angled Trimer	535	648	3.59
Trigonal Trimer	538	611	0.72
L Shape Quadramer	531	663; 608	0.36
Linear Quadrimer	525	680	0.18
Curved Quadrimer	530	671; 617	0.72
Standard Deviation	**4.49**	**27.72**	

A known property of PAA is its ability to swell and expand when exposed to aqueous solutions of neutral pH around 6.5 or 7[149]–[151]. Therefore, the PAA beneath the gold nanoparticles experiences a more compact and denser surface conformation when the surface is dry compared to when exposed to an aqueous solution. These changes in surface conformation of the underlying PAA likely induce changes in the gold nanoparticle deposition profiles, which also need to be taken into consideration in the simulated models. Gold nanoparticles that form clustered arrangements on dry compact PAA surfaces likely deposit in close proximity to neighbouring nanoparticles within a cluster and therefore, would experience small or no inter-nanoparticle gaps. Conversely, under an aqueous environment, the PAA would swell and expand, potentially moving nanoparticles within a cluster further apart. Consequently, when simulating the optical response of the sensor surface, the inter-nanoparticle gaps (or lack-thereof) within clusters would be modified accordingly to accurately represent the nanoparticle deposition profile. A result from varying inter-nanoparticle gaps within the deposited clusters is the changing extinction profile. With a decreasing inter-nanoparticle gap, it was seen that the LSPR of the nanoparticles comprising a cluster are more

strongly coupled together and therefore, result in a red-shifted secondary extinction peak (Figure 21). This is exemplified through the simulated extinction cross sections of a cluster with a trigonal trimer shape with interparticle distances ranging from 1 nm to 5 nm (Figure 21). However, when the interparticle distance was 0 nm, there was a slight blue shift in the secondary extinction peak. This can be explained by the presence of quantum tunneling, which becomes possible at sub-nanometer gaps between the gold nanoparticles. Quantum tunneling can be simply described as the passing of electrons through a potential barrier, without sufficient energy to be achieved in the classic realm. However, using quantum mechanics, there is a non-zero chance that the electrons will successfully "tunnel" through the potential barrier and reach a new location. When the interparticle distance between gold nanoparticles is below 1 nm, this tunneling property comes into effect and electrons are able to travel between the gold nanoparticles. It has previously been demonstrated that quantum-tunneling screens LSPR charges and reduces the amount of plasmonic coupling between the nanoparticles[152]. Therefore, the nanoparticles with interparticle distance of 0 nm experience this quantum-tunneling screening, which explains the slight shift towards shorter wavelengths for the extinction peak observed going from an interparticle distance of 1 nm to 0 nm.

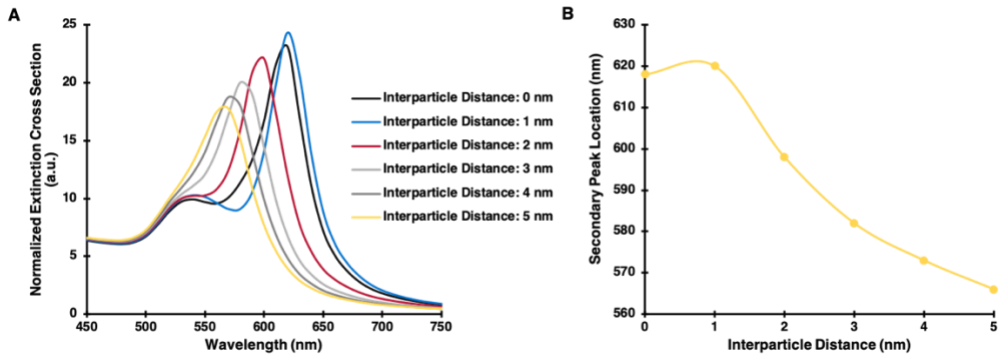

Figure 21. A) Normalized extinction cross section of simulated isolated trigonal trimer cluster with varying interparticle distances exposed to a refractive index of 1.35 B) Secondary peak location of trigonal trimer cluster for varying interparticle distances

To incorporate the PAA swelling and consequent variations in interparticle distances into the simulations, the sensor exposed to an external environment of ambient air, was simulated with interparticle distances of 0 nm, 1 nm and 2 nm with a 0.25, 0.5 and 0.25 weighting. When simulating the sensor surface exposed to an aqueous external environment, the interparticle distances used were 0 nm, 1 nm, 2 nm and 3 nm and given a 0.2, 0.3, 0.3 and 0.2 weighting. When incorporating all the cluster types with the various effective refractive index values, it was demonstrated that the secondary

peaks were affected to a larger degree by the changing interparticle distances compared to the primary peaks (Figure 22). This is expected as the primary peaks correspond to the coupling of light to individual nanoparticles, either as an isolated nanoparticle, or light coupling in a perpendicular direction to the length of the cluster and therefore, would not be significantly affected by the distance of neighbouring nanoparticles. To demonstrate this trend, interparticle distances of ensembles representative of the nanoplasmonic surface were simulated and shown to have consistent primary peak locations of 535 nm for interparticle distances of 0 nm, 1 nm, 2 nm and 3 nm. Whereas the secondary peak locations were 639 nm, 651 nm, 620 nm and 599 nm for interparticle distances of 0 nm, 1 nm, 2 nm and 3 nm respectively with a standard deviation of 22.75 nm.

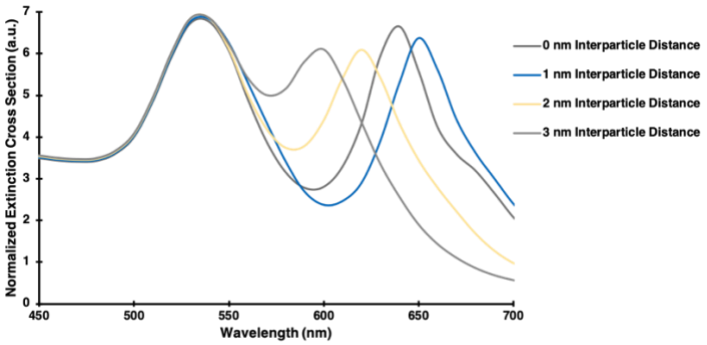

Figure 22. Simulated normalized extinction cross section of gold nanoparticles exposed to an aqueous external environment with a refractive index of 1.33. Incorporated weighted averages of PAA coverage resulting in effective refractive index values of 1.4082, 1.4252 and 1.4422 given weights of 0.25, 0.5 and 0.25 respectively.

It can be concluded that the extinction profile is highly dependent on the degree to which the nanoparticles are exposed to the underlying PAA, the shape of the nanoparticle clusters as well as interparticle distance between the component nanoparticles. However, when comparing the resultant extinction profiles with these variations, the secondary extinction peaks are more heavily influenced by these properties than the primary extinction peaks. Therefore, when the component extinction profiles are summed together to create an overall representation of the nanoplasmonic sensor surface, the secondary peaks experience less overlap than the primary peaks and result in a broader overall spectrum peak. Consequently, when exposed to a higher refractive index, the increase in extinction intensity of the secondary peak is spread out over a larger wavelength range compared to the increase experienced by the primary peak. This resulted in the primary peak appearing to experience a greater

increase in intensity than secondary peak and thus, creating a ratiometric response to the change in refractive index. With the combination of the effective refractive index, shapes prominence and interparticle distances, the simulated trends were similar to those demonstrated experimentally (Figure 23A and B). The red-shifts calculated on the simulated primary peaks were similar to those experimentally observed, being 10 nm and 4 nm compared to 14 nm and 4 nm respectively (Figure 23C). However, the simulated secondary peaks experienced greater shifts than experimentally demonstrated being 29 nm and 12 nm in the simulations and 28 nm and 2 nm experimentally (Figure 23D). Furthermore, the location of the secondary peak is blue-shifted in the simulated spectrum compared to the experimentally determined spectrum, with the peak (when exposed to air) being 609 nm in the simulation as opposed to 666 nm experimentally (Figure 23 D). The discrepancy in the secondary peak locations might be due to the limited sample size that was used in collecting the data on the cluster profile. There might have been a greater portion of large clusters deposited that were not accounted for on the sample images that the cluster profile was based on, rendering a blue-shifted simulated coupled LSPR peak compared to that observed experimentally. Furthermore, it is important to note a source of error in the simulations is the large step size of 10 nm between calculated values. By graphing the points, the expected peak locations can be extrapolated, however the relatively large step size could be a cause for slight inaccuracies in peak location. However, the overall ratiometric trend that was observed in the simulations was consistent with those observed experimentally, confirming that the unique assortment of deposited gold nanoparticles is key in achieving the ratiometric profile in response to refractive index changes (Figure 23D).

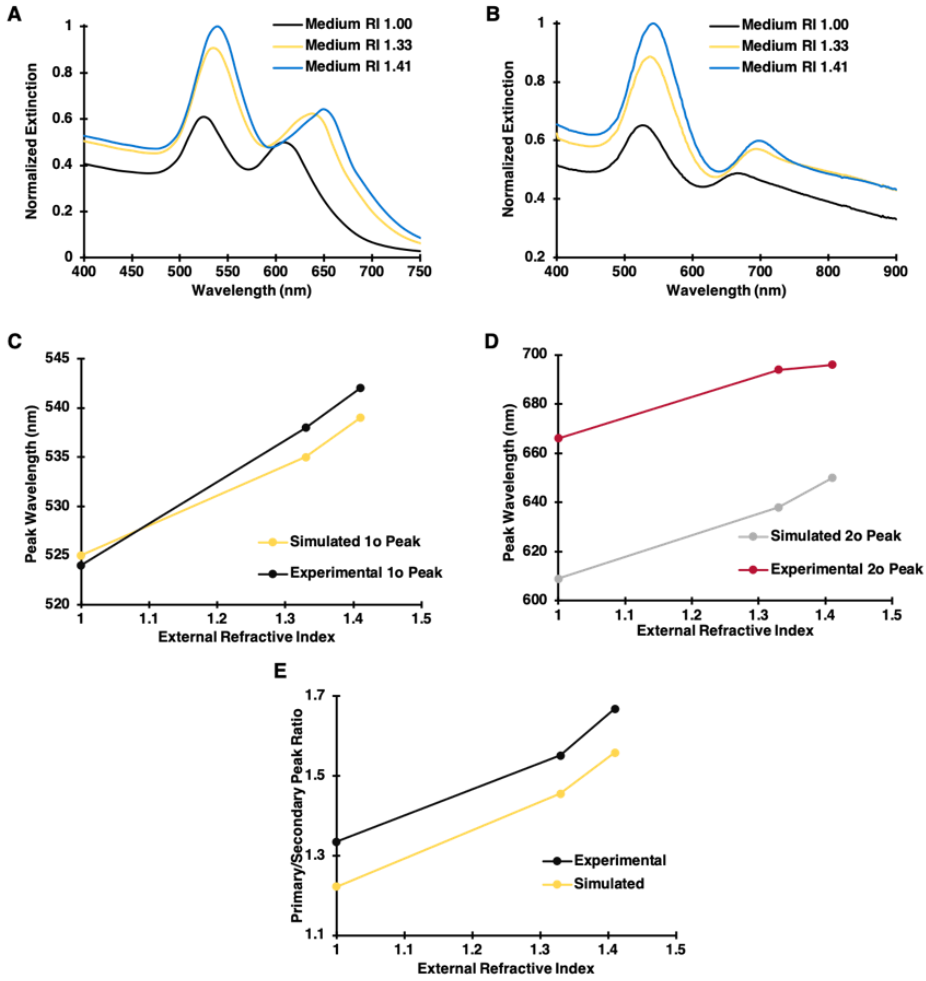

Figure 23 A) Simulated normalized extinction cross section of gold nanoparticles exposed to mediums with a refractive index values of 1.00, 1.33 and 1.41. Incorporated weighted averages of PAA coverage and interparticle distances. B) Peak normalized UV-Vis extinction spectra showing ratiometric response to external refractive index values of 1.00, 1.33, and 1.41. Sensors deposited with gold nanoparticle diameters 43 nm and PAA pH 6. (C-D) Simulated and experimental peak shift in response to refractive index changes for C) Primary peaks D) Secondary peaks E) Primary to secondary peak ratios for simulated and experimentally determined extinction profiles in response to refractive index changes.

5.5 Conclusions

Simulations were conducted in COMSOL Multiphysics that theoretically confirmed the ratiometric responses experimentally achieved. Based on the simulations of the component nanoparticle ensembles, it was determined that the weaker response to refractive index changes exhibited by the secondary peak was caused by unique variabilities in the deposition parameters. It was demonstrated that the coupled LSPR peaks were strongly affected by variations in the effective refractive index values and interparticle distances within clusters. Furthermore, the different cluster shapes that were deposited experienced a wide range of coupled LSPR wavelengths. When all the component nanoparticle ensembles were added together, they resulted in broad secondary extinction peaks, compared to relatively narrow primary extinction peaks, as the uncoupled LSPR were not as affected by the variations in the deposition parameters. Consequently, when exposed to a change in refractive index, the increase in intensity experienced by the secondary peaks was stretched over a larger wavelength range than the primary peaks. This resulted in the secondary peaks exhibiting a lower extinction intensity increase compared to the primary peaks and was responsible for the optical ratiometric response.

Chapter 6
Conclusions and Future Work

6.1 Summary

This thesis presents a new ratiometric nanoplasmonic refractive index sensor that provides visually red shifting colourimetric outputs, which can be interpreted by the naked eye. Beginning with a literature review summarizing refractive index sensing mechanisms that utilize nanotechnology, the nano-scale properties currently exploited for refractive index sensing are established. With this knowledge, gold nanoparticles and nanoclusters were manipulated to achieve a unique optical response to refractive index changes, creating a novel ratiometric and colourimetric signal. This ratiometric response was shown both experimentally and theoretically and was mechanistically explained, providing a novel contribution to existing scientific literature surrounding gold nanoparticles and refractive index sensors.

6.2 Conclusions

A nanoplasmonic ratiometric sensor based on the deposition of static and spherical gold nanoparticle ensembles has been demonstrated that provides a blue to red colourimetric output for increasing refractive index. This is the first time that both single and clustered spherical gold nanoparticles have been immobilized with the intent of creating a colourimetric refractive index sensor. The optical and colourimetric properties of the nanoplasmonic refractive index sensing surface were shown to be regulated by controlling the degree of nanoparticle coupling of the immobilized nanoparticles. By using the novel electrostatic deposition technique implemented in this nanoplasmonic sensor, the degree of nanoparticle coupling was easily regulated without complex nanolithography or microfabrication techniques. This control was gained by varying the pH of the underlying PAA, as well as the size and concentration of the gold nanoparticles used in the deposition step. This allowed for varying ratios of dispersed isolated nanoparticles and aggregated nanoparticle clusters. It was demonstrated that for the varying amounts of single and clustered immobilized nanoparticles, the sensor surfaces all maintained a ratiometric response to the environmental local refractive index. The initial ratios of single to clustered nanoparticles did affect the initial colour of the sensor surface as well as the colour transition experienced in response to refractive index changes. However, all sensor surfaces demonstrated repeatable colourimetric and ratiometric shifts in response to refractive index changes, such that the sensor surfaces could be reused multiple times. Due to the electrostatic nature of the deposition, the attraction of the gold nanoparticles to the sensor surface was vulnerable to ionic and polar solutions that would screen the attractive charges holding the gold nanoparticles onto the sensor surface, therefore, limiting the applications where this sensor could be implemented.

Furthermore, to understand the origin of the ratiometric response to refractive index changes, the component nanoparticle ensembles were simulated independently allowing their contribution to the extinction profile to be isolated and analyzed. The deposition properties that resulted in the ratiometric response were variations in the PAA coverage of the gold nanoparticle surface area, variations in the interparticle distances as well as the deposition of various cluster sizes and shapes. These deposition features created a broad coupled LSPR extinction peak such that the increase in extinction intensity caused by a refractive index change was spread over a large wavelength range. This caused the extinction intensity change to appear to be weaker in the coupled LSPR peaks than in the uncoupled LSPR peaks, which were less sensitive to the deposition parameters mentioned above

and consequently experienced more additive peak intensities. By accounting for the varying deposition properties in the simulations and combining the simulated component nanoparticle ensembles based on their experimentally observed prevalence, a similar ratiometric response was simulated to that achieved experimentally, thus supporting the accuracy of the theoretical explanations.

6.3 Recommendations for Future Work

The current gold nanoparticle sensor benefits from numerous qualities such as ease of fabrication, a wide colourimetric range providing signals decipherable by the naked eye, as well as reusability. However, the current gold nanoparticle deposition method to achieve this optical response uses electrostatic interactions to immobilize the ensemble of gold nanoparticles. Due to the inherent weakness of electrostatic attractions in different environmental solutions and solvents, a more resilient covalent deposition method could be attempted to achieve more robust immobilization. Furthermore, the developed sensor surface is vulnerable to mechanical abrasions and therefore, thin porous overlays could also be attempted to be deposited over the immobilized nanoparticles to increase the durability of the sensor surface and consequently increase its applicability for commercial implementation.

To broaden the applications of this sensor, attempts could be made to fabricate the sensor on various substrate surfaces. Currently, the gold nanoparticle deposition has been achieved on glass surfaces, however, immobilization onto various types of consumer care products and industrial surfaces would further expand its potential for commercial applications. Specifically, there is a need for a colourimetric refractive index sensor that can be deposited inside contact lens cases to detect bacterial biofilms. The primary component in a bacterial biofilm is a matrix of extracellular polymeric substances which has a refractive index around 1.3 and is colourless[153]. Since these biofilms inside contact lens cases protect bacteria from disinfectant solutions used to sterilize contact lenses, they increase the risk of users contracting microbial and infiltrative keratitis[154], [155]. With bacterial contamination documented in over 50% of contact lens cases[154], [155], visually detecting the presence of a bacterial biofilm inside of the contact lens case would provide a huge impact on the ocular health of contact lens wearers. Preliminary experiments were conducted (not shown here) which observed ratiometric shifts on nanoplasmonic surfaces exposed to various bacterial biofilms. Therefore, it is a promising technology to output an easily interpreted signal to alert users of the presence of bacterial biofilms on consumer care surfaces.

Lastly, this sensing mechanism currently experiences a limitation for people who are colourblind and are unable to interpret the optical output for the refractive index measurements. To overcome this obstacle, developing a smartphone application or a portable digital analyzer to interpret the colourimetric response would aid in the accessibility of this sensor as well as potentially improve user compliance.

Bibliography

[1] Y. Khan, A. Li, L. Chang, L. Li, and L. Guo, “Gold nano disks arrays for localized surface plasmon resonance based detection of PSA cancer marker,” *Sensors Actuators, B Chem.*, vol. 255, pp. 1298–1307, 2018.

[2] Y. Hong, E. Lee, M. Ku, J. S. Suh, D. S. Yoon, and J. Yang, “Femto-molar detection of cancer marker-protein based on immuno-nanoplasmonics at single-nanoparticle scale,” *Nanotechnology*, vol. 27, no. 18, p. 0, 2016.

[3] E. M. Girotto, J. P. Monteiro, J. H. de Oliveira, A. G. Brolo, and E. Radovanovic, “Microfluidic Plasmonic Biosensor for Breast Cancer Antigen Detection,” *Plasmonics*, vol. 11, no. 1, pp. 45–51, 2015.

[4] S. Barth *et al.*, “Plasmonic flow-through biosensor using a polymeric substrate,” *J. Micromechanics Microengineering*, vol. 24, no. 3, p. 034001, 2014.

[5] C. Escobedo, “On-chip nanohole array based sensing: A review,” *Lab Chip*, vol. 13, no. 13, pp. 2445–2463, 2013.

[6] Y. Yanase, K. Sakamoto, K. Kobayashi, and M. Hide, “Diagnosis of immediate-type allergy using surface plasmon resonance,” *Opt. Mater. Express*, vol. 6, no. 4, pp. 1339–1348, 2016.

[7] J. R. Zeng, C. C. Cheng, A. W. Lee, P. L. Wei, and J. K. Chen, “Visualization platform of one-dimensional gratings of tethered polyvinyltetrazole brushes on silicon surfaces for sensing of Cr(III),” *Microchim. Acta*, vol. 184, no. 8, pp. 2723–2730, 2017.

[8] J. R. Zeng, C. C. Cheng, B. R. Huang, C. H. Huang, and J. K. Chen, “Pillar arrays of tethered polyvinyltetrazole on silicon as a visualization platform for sensing of lead ions,” *Sensors Actuators, B Chem.*, vol. 243, pp. 234–243, 2017.

[9] B. D. Spangler, E. A. Wilkinson, J. T. Murphy, and B. J. Tyler, “Comparison of the Spreeta® surface plasmon resonance sensor and a quartz crystal microbalance for detection of Escherichia coli heat-labile enterotoxin,” *Anal. Chim. Acta*, vol. 444, no. 1, pp. 149–161, 2001.

[10] S. Balasubramanian, I. B. Sorokulova, V. J. Vodyanoy, and A. L. Simonian, “Lytic phage as a specific and selective probe for detection of Staphylococcus aureus-A surface plasmon resonance spectroscopic study,” *Biosens. Bioelectron.*, vol. 22, no. 6, pp. 948–955, 2007.

[11] Ö. Torun, I. Hakki Boyaci, E. Temür, and U. Tamer, “Comparison of sensing strategies in SPR biosensor for rapid and sensitive enumeration of bacteria,” *Biosens. Bioelectron.*, vol. 37, no. 1, pp. 53–60, 2012.

[12] J. Waswa, J. Irudayaraj, and C. DebRoy, “Direct detection of E. Coli O157:H7 in selected food systems by a surface plasmon resonance biosensor,” *LWT - Food Sci. Technol.*, vol. 40, no. 2, pp. 187–192, 2007.

[13] J. Hu, K. Fu, and P. W. Bohn, “Whole-Cell Pseudomonas aeruginosa Localized Surface Plasmon Resonance Aptasensor,” *Anal. Chem.*, vol. 90, no. 3, pp. 2326–2332, 2018.

[14] S. M. Yoo, D.-K. Kim, and S. Y. Lee, “Aptamer-functionalized localized surface plasmon resonance sensor for the multiplexed detection of different bacterial species,” *Talanta*, vol. 132, pp. 112–117, Jan. 2015.

[15] C. Jesus, P. Caldas, O. Frazão, J. L. Santos, P. A. S. Jorge, and J. M. Baptista, “Simultaneous measurement of refractive index and temperature using a hybrid fiber bragg grating/long-period fiber grating configuration,” *Fiber Integr. Opt.*, vol. 28, no. 6, pp. 440–449, 2009.

[16] Q. Wu, Y. Ma, L. Bo, P. Wang, Y. Semenova, and G. Farrell, “Singlemode hetero-core fiber based refractometer demodulated in a ratiometric system,” *Proc. IEEE Sensors*, no. 1, pp. 402–404, 2011.

[17] C. Gouveia, G. Chesini, C. M. B. Cordeiro, J. M. Baptista, and P. A. S. Jorge, “Simultaneous measurement of refractive index and temperature using multimode interference inside a high birefringence fiber loop mirror,” *Sensors Actuators, B Chem.*, vol. 177, pp. 717–723, 2013.

[18] A. F. Coskun, A. E. Cetin, B. C. Galarreta, D. A. Alvarez, H. Altug, and A. Ozcan, “Lensfree optofluidic plasmonic sensor for real-time and label-free monitoring of molecular binding events over a wide field-of-view,” *Sci. Rep.*, vol. 4, pp. 1–7, 2014.

[19] R. Shugayev and P. Bermel, “Propagation Loss-Immune Biocompatible Nanodiamond Refractive Index Sensors,” *Adv. Opt. Mater.*, vol. 6, no. 5, pp. 1–7, 2018.

[20] Y. Tang *et al.*, “Numerical Study of Novel Ratiometric Sensors Based on Plasmon–Exciton Coupling,” *Appl. Spectrosc.*, vol. 71, no. 10, pp. 2377–2384, 2017.

[21] S. N. Kasarova, N. G. Sultanova, and I. D. Nikolov, “Temperature dependence of refractive characteristics of optical plastics,” *J. Phys. Conf. Ser.*, vol. 253, no. 1, 2010.

[22] X. Deng, G. Chen, Q. Peng, Z. Li, J. Meng, and J. Liu, “Research on the fiber Bragg grating sensor for the shock stress measurement,” *Rev. Sci. Instrum.*, vol. 82, no. 10, 2011.

[23] C. Huber, B. Stein, and H. Kalt, “Plasma-enhanced chemical vapor deposition of amorphous silicon carbonitride: Deposition temperature dependence of bonding structure, refractive index, mechanical stress and their aging under ambient air,” *Thin Solid Films*, vol. 634, pp. 66–72, 2017.

[24] Z. Y. Wang *et al.*, “The impact of thickness and thermal annealing on refractive index for aluminum oxide thin films deposited by atomic layer deposition,” *Nanoscale Res. Lett.*, vol. 10, no. 1, 2015.

[25] Y. Yanase, H. Suzuki, T. Tsutsui, T. Hiragun, Y. Kameyoshi, and M. Hide, “The SPR signal in living cells reflects changes other than the area of adhesion and the formation of cell constructions,” *Biosens. Bioelectron.*, vol. 22, no. 6, pp. 1081–1086, 2007.

[26] K. Ishii, H. Suzuki, M. Hide, Y. Yanase, T. Hiragun, and T. Tsutsui, “Applying Surface Plasmon Resonance to Monitor the IgE-Mediated Activation of Human Basophils,” *Allergol. Int.*, vol. 57, no. 4, pp. 347–358, 2008.

[27] J. Homola, S. S. Yee, and G. Gauglitz, “Surface plasmon resonance sensors: review,” *Sensors Actuators B*, vol. 54, pp. 3–15, 1999.

[28] S. Roh, T. Chung, and B. Lee, “Overview of the characteristics of micro- and nano-structured surface plasmon resonance sensors,” *Sensors*, vol. 11, no. 2, pp. 1565–1588, 2011.

[29] I. Abdulhalim, “Plasmonic sensing using metallic nano-sculptured thin films,” *Small*, vol. 10, no. 17, pp. 3499–3514, 2014.

[30] D. S. Wang and S. K. Fan, “Microfluidic surface plasmon resonance sensors: From principles to point-of-care applications,” *Sensors (Switzerland)*, vol. 16, no. 8, 2016.

[31] A. Shalabney, C. Khare, B. Rauschenbach, and I. Abdulhalim, “Sensitivity of surface plasmon resonance sensors based on metallic columnar thin films in the spectral and angular interrogations,” *Sensors Actuators, B Chem.*, vol. 159, no. 1, pp. 201–212, 2011.

[32] D. Maystre, N.-A. P. Nicorovici, C. J. Alleyne, A. G. Kirk, and R. C. McPhedran, “Enhanced SPR sensitivity using periodic metallic structures,” *Opt. Express*, vol. 15, no. 13, p. 8163, 2007.

[33] K. M. Byun, S. M. Jang, S. J. Kim, and D. Kim, “Effect of target localization on the sensitivity of a localized surface plasmon resonance biosensor based on subwavelength metallic nanostructures,” *J. Opt. Soc. Am. A*, vol. 26, no. 4, p. 1027, 2009.

[34] A. Verma, A. Prakash, and R. Tripathi, “Sensitivity improvement of graphene based surface plasmon resonance biosensors with chaclogenide prism,” *Optik (Stuttg).*, vol. 127, no. 4, pp. 1787–1791, 2016.

[35] C. J. Heo *et al.*, “Robust plasmonic sensors based on hybrid nanostructures with facile tunability,” *J. Mater. Chem.*, vol. 22, no. 28, pp. 13903–13907, 2012.

[36] K. Bhattarai *et al.*, “A Large-Area, Mushroom-Capped Plasmonic Perfect Absorber: Refractive Index Sensing and Fabry-Perot Cavity Mechanism,” *Adv. Opt. Mater.*, vol. 3, no. 12, pp. 1779–1786, 2015.

[37] N. Bhalla, S. Sathish, C. J. Galvin, R. A. Campbell, A. Sinha, and A. Q. Shen, “Plasma-Assisted Large-Scale Nanoassembly of Metal-Insulator Bioplasmonic Mushrooms,” *ACS Appl. Mater. Interfaces*, vol. 10, no. 1, pp. 219–226, 2018.

[38] J. Fan, Z. Li, Z. Chen, and W. Wu, “Standing-wave resonances in plasmonic nanoumbrella cavities for color generation and colorimetric refractive index sensor,” *Appl. Surf. Sci.*, vol. 384, pp. 534–538, 2016.

[39] M. Khorasaninejad, S. Mohsen Raeis-Zadeh, H. Amarloo, N. Abedzadeh, S. Safavi-Naeini, and S. S. ing. Saini, “Colorimetric sensors using nano-patch surface plasmon resonators,” *Nanotechnology*, vol. 24, no. 35, p. 355501, 2013.

[40] D. J. Kosciolek *et al.*, “Handheld highly selective plasmonic chem/biosensor using engineered binding proteins for extreme conformational changes,” in *SPIE Nanoscience + Engineering*, 2017, p. 10346.

[41] J. Luan, R. Hu, S. Tadepalli, J. J. Morrissey, E. D. Kharasch, and S. Singamaneni, “Amplification of Refractometric Biosensor Response through Biomineralization of Metal–Organic Framework Nanocrystals,” *Adv. Mater. Technol.*, vol. 2, no. 7, p. 1700023, 2017.

[42] R. A. M. Ali *et al.*, “One-step nanoimprinted hybrid micro-/nano-structure for in situ protein detection of isolated cell array via localized surface plasmon resonance,” *Jpn. J. Appl. Phys.*, vol. 57, no. 3, 2018.

[43] R. Mudachathi and T. Tanaka, “Design of a colorimetric sensing platform using reflection mode plasmonic colour filters,” *Proc. SPIE - Int. Soc. Opt. Eng.*, vol. 10346, no. August, 2017.

[44] E. M. Girotto *et al.*, “Cost-effective plasmonic device for label-free streptavidin detection,” *Mater. Lett.*, vol. 227, pp. 243–246, 2018.

[45] S. Seo, M. R. Gartia, and G. L. Liu, “Vertically stacked plasmonic nanoparticles in a circular arrangement: A key to colorimetric refractive index sensing,” *Nanoscale*, vol. 6, no. 20, pp. 11795–11802, 2014.

[46] N. Sun, J. Cui, Y. She, L. Lu, J. Zheng, and Z. Ye, “Tunable spectral filters based on metallic nanowire gratings,” *Opt. Mater. Express*, vol. 5, no. 4, p. 912, 2015.

[47] A. Campu *et al.*, “Gold NanoBipyramids Performing as Highly Sensitive Dual-Modal Optical Immunosensors,” *Anal. Chem.*, vol. 90, no. 14, pp. 8567–8575, 2018.

[48] E. Hao and G. C. Schatz, “Electromagnetic fields around silver nanoparticles and dimers,” *J. Chem. Phys.*, vol. 120, no. 1, pp. 357–366, 2004.

[49] J. Fu, B. Park, and Y. Zhao, “Limitation of a localized surface plasmon resonance sensor for Salmonella detection,” *Sensors Actuators, B Chem.*, vol. 141, no. 1, pp. 276–283, 2009.

[50] H. R. Culver, M. E. Wechsler, and N. A. Peppas, “Label-Free Detection of Tear Biomarkers Using Hydrogel-Coated Gold Nanoshells in a Localized Surface Plasmon Resonance-Based Biosensor,” *ACS Nano*, vol. 12, no. 9, pp. 9342–9354, 2018.

[51] J. P. Monteiro, S. M. Predabon, C. T. P. Da Silva, E. Radovanovic, and E. M. Girotto, “Plasmonic device based on a PAAm hydrogel/gold nanoparticles composite,” *J. Appl. Polym. Sci.*, vol. 132, no. 34, pp. 1–6, 2015.

[52] N. F. Chiu, C. J. Cheng, and T. Y. Huang, “Organic plasmon-emitting diodes for detecting refractive index variation,” *Sensors*, vol. 13, no. 7, pp. 8340–8351, 2013.

[53] J. Walia, N. Dhindsa, M. Khorasaninejad, and S. S. Saini, “Color generation and refractive index sensing using diffraction from 2D silicon nanowire arrays,” *Small*, vol. 10, no. 1, pp. 144–151, 2014.

[54] M. Khorasaninejad, N. Abedzadeh, J. Walia, S. Patchett, and S. S. Saini, “Color matrix refractive index sensors using coupled vertical silicon nanowire arrays,” *Nano Lett.*, vol. 12,

no. 8, pp. 4228–4234, 2012.

[55] I. Khodadad, N. Dhindsa, and S. S. Saini, “Refractometric Sensing Using High-Order Diffraction Spots from Ordered Vertical Silicon Nanowire Arrays,” *IEEE Photonics J.*, vol. 8, no. 2, 2016.

[56] H. Godwin, “The biological chemistry of lead,” *Curr. Opin. Chem. Biol.*, vol. 5, pp. 223–227, 2001.

[57] H. Needleman, “Lead Poisoning,” *Annu. Rev. Med.*, vol. 55, no. 1, pp. 209–222, Feb. 2004.

[58] S. Mishra and R. N. Bharagava, “Toxic and genotoxic effects of hexavalent chromium in environment and its bioremediation strategies,” *J. Environ. Sci. Heal. - Part C Environ. Carcinog. Ecotoxicol. Rev.*, vol. 34, no. 1, pp. 1–32, 2016.

[59] H. A. Bethe, “Theory of diffraction by small holes,” *Phys. Rev.*, vol. 66, no. 7–8, pp. 163–182, 1944.

[60] T. W. Ebbesen, H. J. Lezec, H. F. Ghaemi, and T. Thio, “Extraordinary optical transmission through sub-wavelength hole arrays,” *Nature*, vol. 391, pp. 667–669, 1998.

[61] C. Genet and T. W. Ebbesen, “Light in tiny holes,” *Nature*, vol. 445, no. 7123, pp. 39–46, 2007.

[62] L. Martín-Moreno *et al.*, “Theory of extraordinary optical transmission through subwavelength hole arrays,” *Phys. Rev. Lett.*, vol. 86, no. 6, pp. 1114–1117, 2001.

[63] H. Liu and P. Lalanne, “Microscopic theory of the extraordinary optical transmission,” *Nature*, vol. 452, pp. 728–731, 2008.

[64] K. A. Tetz, L. Pang, and Y. Fainman, “High-resolution surface plasmon resonance sensor based on linewidth-optimized nanohole array transmittance,” *Opt. Lett.*, vol. 31, no. 10, pp. 1528–1530, 2006.

[65] D. Langley, E. Balaur, C. Sadatnajafi, and B. Abbey, “Dual pitch plasmonic devices for polarization enhanced colour based sensing,” *Proc. SPIE BioPhotonics Australas.*, vol. 10013, p. 1001338, 2016.

[66] M. Soler, A. Belushkin, A. Cavallini, C. Kebbi-Beghdadi, G. Greub, and H. Altug, “Multiplexed nanoplasmonic biosensor for one-step simultaneous detection of Chlamydia

trachomatis and Neisseria gonorrhoeae in urine," *Biosens. Bioelectron.*, vol. 94, pp. 560–567, 2017.

[67] J. Kee, S. Lim, A. Perera, Y. Zhang, and M. Park, "Plasmonic nanohole arrays for monitoring growth of bacteria and antibiotic susceptibility test," *Sensors Actuators B Chem.*, vol. 182, pp. 576–583, 2013.

[68] L. P. Hackett, S. Seo, S. Kim, L. L. Goddard, and G. L. Liu, "Label-free cell-substrate adhesion imaging on plasmonic nanocup arrays," *Biomed. Opt. Express*, vol. 8, no. 2, p. 1139, 2017.

[69] D. Zhang *et al.*, "Peptide functionalized nanoplasmonic sensor for explosive detection," *Nano-Micro Lett.*, vol. 8, no. 1, pp. 36–43, 2016.

[70] M. R. Gartia *et al.*, "Colorimetric Plasmon Resonance Imaging Using Nano Lycurgus Cup Arrays," *Adv. Opt. Mater.*, vol. 1, no. 1, pp. 68–76, 2013.

[71] X. Wang, T. W. Chang, G. Lin, M. R. Gartia, and G. L. Liu, "Self-Referenced Smartphone-Based Nanoplasmonic Imaging Platform for Colorimetric Biochemical Sensing," *Anal. Chem.*, vol. 89, no. 1, pp. 611–615, 2017.

[72] L. Varga, E. Thiry, and G. Füst, "BSA-anti-BSA immune complexes formed in the presence of human complement do not bind to autologous red blood cells," *Immunology*, vol. 64, pp. 381–384, 1988.

[73] A. G. Brolo *et al.*, "Attomolar Protein Detection Using in-Hole Surface Plasmon Resonance," *J. Am. Chem. Soc.*, vol. 131, no. 2, pp. 436–437, 2009.

[74] C. Escobedo, A. G. Brolo, R. Gordon, and D. Sinton, "Flow-through vs flow-over: Analysis of transport and binding in nanohole array plasmonic biosensors," *Anal. Chem.*, vol. 82, no. 24, pp. 10015–10020, 2010.

[75] Y. Zhao, G. Gaur, S. T. Retterer, P. E. Laibinis, and S. M. Weiss, "Flow-through porous silicon membranes for real-time label-free biosensing," *Anal. Chem.*, vol. 88, no. 22, pp. 10940–10948, 2016.

[76] A. A. Yanik, M. Huang, A. Artar, T. Y. Chang, and H. Altug, "Integrated nanoplasmonic-nanofluidic biosensors with targeted delivery of analytes," *Appl. Phys. Lett.*, vol. 96, no. 2, p. 021101, 2010.

[77] A. A. Yanik *et al.*, “An optofluidic nanoplasmonic biosensor for direct detection of live viruses from biological media,” *Nano Lett.*, vol. 10, no. 12, pp. 4962–4969, 2010.

[78] S. Gavilanes-Parra, J. Gomez-Cruz, C. Escobedo, A. Manjarrez-Hernandez, S. Nair, and G. Ascanio, “Cost-effective flow-through nanohole array-based biosensing platform for the label-free detection of uropathogenic E. coli in real time,” *Biosens. Bioelectron.*, vol. 106, pp. 105–110, 2018.

[79] H. Im, N. J. Wittenberg, A. Lesuffleur, N. C. Lindquist, and S. H. Oh, “Membrane protein biosensing with plasmonic nanopore arrays and pore-spanning lipid membranes,” *Chem. Sci.*, vol. 1, no. 6, pp. 688–696, 2010.

[80] J. A. Jackman *et al.*, “Plasmonic Nanohole Sensor for Capturing Single Virus-Like Particles toward Virucidal Drug Evaluation,” *Small*, vol. 12, no. 9, pp. 1159–1166, 2016.

[81] A. G. Brolo *et al.*, “Nanoholes As Nanochannels: Flow-through Plasmonic Sensing,” *Anal. Chem.*, vol. 81, no. 11, pp. 4308–4311, 2009.

[82] C. Escobedo *et al.*, “Integrated nanohole array surface plasmon resonance sensing device using a dual-wavelength source,” *J. Micromechanics Microengineering*, vol. 21, no. 11, p. 115001, 2011.

[83] J. Gomez, S. Nair, G. Ascanio, and C. Escobedo, “Flow-through nanohole array based sensor implemented on analogue smartphone components,” in *Plasmonics: Design, Materials, Fabrication, Characterization, and Applications XV*, 2017, vol. 10346.

[84] K. Iwai, R. D. Sochol, L. P. Lee, and L. Lin, “Finger-powered bead-in-droplet microfluidic system for point-of-care diagnostics,” in *Proceedings of the IEEE International Conference on Micro Electro Mechanical Systems (MEMS)*, 2012, no. February, pp. 949–952.

[85] A. Asseh, R. Stubbe, H. Ahlfeldt, B. Sahlgren, R. Stubbe, and G. Edwall, “Fiber optical Bragg grating refractometer,” *Fiber Integr. Opt.*, vol. 17, pp. 51–62, 1998.

[86] K. Schroeder, W. Ecke, R. Mueller, R. Willsch, and A. Andreev, “A fibre Bragg grating refractometer,” *Meas. Sci. Technol.*, vol. 12, no. 7, pp. 757–764, 2001.

[87] Y. Liu, C. Meng, A. P. Zhang, Y. Xiao, H. Yu, and L. Tong, “Compact microfiber Bragg gratings with high-index contrast,” *Opt. Lett.*, vol. 36, no. 16, pp. 3115–3117, 2011.

[88] D. Sun, T. Guo, Y. Ran, Y. Huang, and B. O. Guan, “In-situ DNA hybridization detection

with a reflective microfiber grating biosensor," *Biosens. Bioelectron.*, vol. 61, pp. 541–546, 2014.

[89] M. Yang, D. N. Wang, and C. R. Liao, "Fiber Bragg grating with micro-holes for simultaneous and independent refractive index and temperature sensing," *Photonics Technol. Lett.*, vol. 23, no. 20, pp. 1511–1513, 2011.

[90] A. Singh, "Various characteristics of long-period fiber grating-based refractive index sensor," *Optik (Stuttg).*, vol. 126, no. 24, pp. 5439–5443, 2015.

[91] Q. Shi and B. T. Kuhlmey, "Optimization of photonic bandgap fiber long period grating refractive-index sensors," *Opt. Commun.*, vol. 282, no. 24, pp. 4723–4728, 2009.

[92] C. W. Wu, C. Y. Chiang, C. H. Chen, C. S. Chiang, C. T. Wang, and L. K. Chau, "Self-referencing fiber optic particle plasmon resonance sensing system for real-time biological monitoring," *Talanta*, vol. 146, pp. 291–298, 2016.

[93] J. M. Trudeau *et al.*, "Combined fibre-optic sensor for colour and refractive index (CI) monitoring," *Meas. Sci. Technol.*, vol. 17, no. 5, pp. 1134–1139, 2006.

[94] M. I. Zibaii, A. Kazemi, H. Latifi, M. K. Azar, S. M. Hosseini, and M. H. Ghezelaiagh, "Measuring bacterial growth by refractive index tapered fiber optic biosensor," *J. Photochem. Photobiol. B Biol.*, vol. 101, no. 3, pp. 313–320, 2010.

[95] T. Hu, Y. Zhao, and L. Cai, "Temperature and refractive index sensor using a high-birefringence fiber loop mirror and single mode-coreless-single mode fiber structure," *Instrum. Sci. Technol.*, vol. 44, no. 4, pp. 366–376, 2016.

[96] A. Mukherjee *et al.*, "Characterization of a fiber optic liquid refractive index sensor," *Sensors Actuators, B Chem.*, vol. 145, no. 1, pp. 265–271, 2010.

[97] H. W. Lee *et al.*, "Optofluidic refractive-index sensor in step-index fiber with parallel hollow micro-channel," *Opt. Express*, vol. 19, no. 9, p. 8200, 2011.

[98] J. Burgmeier, A. Feizpour, W. Schade, and B. M. Reinhard, "Plasmonic nanoshell functionalized etched fiber Bragg gratings for highly sensitive refractive index measurements," *Opt. Lett.*, vol. 40, no. 4, pp. 546–549, 2015.

[99] H. Suzuki, M. Sugimoto, Y. Matsui, and J. Kondoh, "Fundamental characteristics of a dual-colour fibre optic SPR sensor," *Meas. Sci. Technol.*, vol. 17, no. 6, pp. 1547–1552, 2006.

[100] H. Suzuki, M. Sugimoto, Y. Matsui, and J. Kondoh, “Development of a dual-color optical fiber SPR sensor,” *Proc. IEEE Sensors*, vol. 2005, pp. 865–868, 2005.

[101] R. Gupta and N. J. Goddard, “Optical waveguide for common path simultaneous refractive index and broadband absorption measurements in small volumes,” *Sensors Actuators, B Chem.*, vol. 237, pp. 1066–1075, 2016.

[102] J.-H. Li, C.-L. Zhao, and C.-K. Ji, “Simultaneous multi-point measurement of refractive index using optical fiber sensor based on an arrayed-waveguide grating,” in *22nd International Conference on Optical Fiber Sensors*, 2012, vol. 8421, pp. 84219N-84219N–4.

[103] M. Id *et al.*, “Refractive index sensing in rectangular glass micro-capillaries by spectral reflectivity measurements,” *J. Sel. Top. QUANTUM Electron.*, vol. 22, no. 3, 2015.

[104] I. Del Villar, I. R. Matias, F. J. Arregui, and P. Lalanne, “Optimization of sensitivity in Long Period Fiber Gratings with overlay deposition,” *Opt. Express*, vol. 13, no. 1, pp. 56–69, 2005.

[105] P. Pilla *et al.*, “Long period grating working in transition mode as promising technological platform for label-free biosensing,” *Opt. Express*, vol. 17, no. 22, p. 20039, 2009.

[106] F. Chiavaioli *et al.*, “Sol-Gel-Based Titania-Silica Thin Film Overlay for Long Period Fiber Grating-Based Biosensors,” *Anal. Chem.*, vol. 87, no. 24, pp. 12024–12031, 2015.

[107] J.-M. Renoirt, C. Zhang, M. Debliquy, M.-G. Olivier, P. Mégret, and C. Caucheteur, “High-refractive-index transparent coatings enhance the optical fiber cladding modes refractometric sensitivity,” *Opt. Express*, vol. 21, no. 23, p. 29073, 2013.

[108] B. N. Shivananju, M. Renilkumar, G. R. Prashanth, S. Asokan, and M. M. Varma, “Detection limit of etched fiber bragg grating sensors,” *J. Light. Technol.*, vol. 31, no. 14, pp. 2441–2447, 2013.

[109] Q. Li *et al.*, “Enhanced sucrose sensing sensitivity of long period fiber grating by self-assembled polyelectrolyte multilayers,” *React. Funct. Polym.*, vol. 71, no. 3, pp. 335–339, 2011.

[110] Y. Y. Shevchenko and J. Albert, “Plasmon resonances in gold-coated tilted fiber Bragg gratings,” *Opt. Lett.*, vol. 32, no. 3, pp. 211–213, 2007.

[111] T. Schuster, R. Herschel, N. Neumann, and C. G. Schäffer, “Miniaturized long-period fiber grating assisted surface plasmon resonance sensor,” *J. Light. Technol.*, vol. 30, no. 8, pp.

1003–1008, 2012.

[112] M. C. Phan Huy *et al.*, “Tilted Fiber Bragg Grating photowritten in microstructured optical fiber for improved refractive index measurement,” *Opt. Express*, vol. 14, no. 22, pp. 10359–10370, 2006.

[113] M. C. Phan Huy *et al.*, “Three-hole microstructured optical fiber for efficient fiber Bragg grating refractometer,” *Opt. Lett.*, vol. 32, no. 16, pp. 2390–2392, 2007.

[114] M. Calcerrada, C. García-Ruiz, and M. González-Herráez, “Chemical and biochemical sensing applications of microstructured optical fiber-based systems,” *Laser Photonics Rev.*, vol. 9, no. 6, pp. 604–627, 2015.

[115] P. Pilla *et al.*, “A protein-based biointerfacing route toward label-free immunoassays with long period gratings in transition mode,” *Biosens. Bioelectron.*, vol. 31, no. 1, pp. 486–491, 2012.

[116] S. Sridevi, K. S. Vasu, S. Asokan, and A. K. Sood, “Sensitive detection of C-reactive protein using optical fiber Bragg gratings,” *Biosens. Bioelectron.*, vol. 65, pp. 251–256, 2015.

[117] S. Sridevi, K. S. Vasu, N. Jayaraman, S. Asokan, and A. K. Sood, “Optical bio-sensing devices based on etched fiber Bragg gratings coated with carbon nanotubes and graphene oxide along with a specific dendrimer,” *Sensors Actuators, B Chem.*, vol. 195, pp. 150–155, 2014.

[118] S. Korposh, R. Selyanchyn, W. Yasukochi, S. W. Lee, S. W. James, and R. P. Tatam, “Optical fibre long period grating with a nanoporous coating formed from silica nanoparticles for ammonia sensing in water,” *Mater. Chem. Phys.*, vol. 133, no. 2–3, pp. 784–792, 2012.

[119] K. Dandapat, S. M. Tripathi, Y. Chinifooroshan, W. J. Bock, and P. Mikulic, “Compact and cost-effective temperature-insensitive bio-sensor based on long-period fiber gratings for accurate detection of E coli bacteria in water,” *Opt. Lett.*, vol. 41, no. 18, pp. 4198–4201, 2016.

[120] M. Smietana, W. J. Bock, P. Mikulic, A. Ng, R. Chinnappan, and M. Zourob, “Detection of bacteria using bacteriophages as recognition elements immobilized on long-period fiber gratings,” *Opt. Express*, vol. 19, no. 9, pp. 7971–7978, 2011.

[121] S. M. Tripathi *et al.*, “Long period grating based biosensor for the detection of Escherichia coli bacteria,” *Biosens. Bioelectron.*, vol. 35, no. 1, pp. 308–312, 2012.

[122] A. B. Bandara, Z. Zuo, S. Ramachandran, A. Ritter, J. R. Heflin, and T. J. Inzana, “Detection of methicillin-resistant staphylococci by biosensor assay consisting of nanoscale films on optical fiber long-period gratings,” *Biosens. Bioelectron.*, vol. 70, pp. 433–440, 2015.

[123] M. Kutscher *et al.*, “Surface functionalization allowing repetitive use of optical sensors for real-time detection of antibody-bacteria interaction,” *J. Biophotonics*, vol. 9, no. 7, pp. 730–737, 2016.

[124] D. Bhatta, E. Stadden, E. Hashem, I. J. G. Sparrow, and G. D. Emmerson, “Multi-purpose optical biosensors for real-time detection of bacteria, viruses and toxins,” *Sensors Actuators B Chem.*, vol. 149, no. 1, pp. 233–238, 2010.

[125] D. Bhatta, E. Stadden, E. Hashem, I. J. G. Sparrow, and G. D. Emmerson, “Label-free monitoring of antibody-antigen interactions using optical microchip biosensors,” *J. Immunol. Methods*, vol. 362, no. 1–2, pp. 121–126, 2010.

[126] M. Marti Villalba *et al.*, “Optical microchip array biosensor for multiplexed detection of bio-hazardous agents,” *Biosens. Bioelectron.*, vol. 30, no. 1, pp. 78–86, 2011.

[127] F. Chiavaioli, F. Baldini, S. Tombelli, C. Trono, and A. Giannetti, “Biosensing with optical fiber gratings,” *Nanophotonics*, vol. 6, no. 4, pp. 663–679, 2017.

[128] D. Mabey, R. W. Peeling, A. Ustianowski, and M. D. Perkins, “Diagnostics for the developing world,” *Nat. Rev. Microbiol.*, vol. 2, no. 3, pp. 231–240, 2004.

[129] M. S. Verma, P. Z. Chen, L. Jones, and F. X. Gu, “Branching and size of CTAB-coated gold nanostars control the colorimetric detection of bacteria,” *RSC Adv.*, vol. 4, no. 21, p. 10660, 2014.

[130] P. Bieker and M. Schönhoff, “Linear and exponential growth regimes of multilayers of weak polyelectrolytes in dependence on pH,” *Macromolecules*, vol. 43, no. 11, pp. 5052–5059, 2010.

[131] J. Choi and M. F. Rubner, “Influence of the degree of ionization on weak polyelectrolyte multilayer assembly,” *Macromolecules*, vol. 38, no. 1, pp. 116–124, 2005.

[132] S. S. Shiratori and M. F. Rubner, “pH-dependent thickness behavior of sequentially adsorbed layers of weak polyelectrolytes,” *Macromolecules*, vol. 33, no. 11, pp. 4213–4219, 2000.

[133] D. Yoo, S. S. Shiratori, and M. F. Rubner, “Controlling bilayer composition and surface

wettability of sequentially adsorbed multilayers of weak polyelectrolytes," *Macromolecules*, vol. 31, no. 13, pp. 4309–4318, 1998.

[134] S. E. Burke and C. J. Barrett, "Acid-base equilibria of weak polyelectrolytes in multilayer thin films," *Langmuir*, vol. 19, no. 8, pp. 3297–3303, 2003.

[135] C. Bohren and D. Huffman, "Absorption and Scattering of Light by Small Particles," C. F. Bohren and D. R. Huffman, Eds. Weinheim, Germany: New York:Wiley, 1983, p. 530 pp.

[136] E. Petryayeva and U. J. Krull, "Localized surface plasmon resonance: Nanostructures, bioassays and biosensing-A review," *Anal. Chim. Acta*, vol. 706, no. 1, pp. 8–24, 2011.

[137] J. S. Sekhon and S. S. Verma, "Refractive Index Sensitivity Analysis of Ag, Au, and Cu Nanoparticles," *Plasmonics*, vol. 6, no. 2, pp. 311–317, 2011.

[138] C. Novo, A. M. Funston, I. Pastoriza-Santos, L. M. Liz-Marzán, and P. Mulvaney, "Influence of the medium refractive index on the optical properties of single gold triangular prisms on a substrate," *J. Phys. Chem. C*, vol. 112, no. 1, pp. 3–7, 2008.

[139] N. J. Halas, S. Lal, W. S. Chang, S. Link, and P. Nordlander, "Plasmons in strongly coupled metallic nanostructures," *Chem. Rev.*, vol. 111, no. 6, pp. 3913–3961, 2011.

[140] S. A. Maier, M. L. Brongersma, P. G. Kik, and H. A. Atwater, "Observation of near-field coupling in metal nanoparticle chains using far-field polarization spectroscopy," *Phys. Rev. B*, vol. 65, no. 19, p. 193408, 2002.

[141] P. K. Jain, W. Huang, and M. A. El-Sayed, "On the universal scaling behavior of the distance decay of plasmon coupling in metal nanoparticle pairs: A plasmon ruler equation," *Nano Lett.*, vol. 7, no. 7, pp. 2080–2088, 2007.

[142] P. K. Jain and M. A. El-Sayed, "Plasmonic coupling in noble metal nanostructures," *Chem. Phys. Lett.*, vol. 487, no. 4–6, pp. 153–164, 2010.

[143] M. W. Knight, Y. Wu, J. B. Lassiter, P. Nordlander, and N. J. Halas, "Substrates matter: influence of an adjacent dielectric on an individual plasmonic nanoparticle," *Nano Lett.*, vol. 9, no. 5, pp. 2188–2192, 2009.

[144] L. Novotny, B. Hecht, and O. Keller, "Principles of Nano-Optics," *Phys. Today*, vol. 60, no. 7, p. 62, Jul. 2007.

[145] Y. Wu and P. Nordlander, “Finite-Difference Time-Domain Modeling of the Optical Properties of Nanoparticles near DIelectric Substrates,” *J. Phys. Chem.*, vol. 114, no. 713, pp. 7302–7307, 2010.

[146] C. L. Du, S. Peng, W. C. Yang, and D. N. Shi, “Plasmonic Coupling Effects on the Refractive Index Sensitivities of Plane Au-Nanosphere-Cluster Sensors,” *Plasmonics*, vol. 13, no. 5, pp. 1729–1734, 2018.

[147] P. K. Jain and M. A. El-Sayed, “Noble metal nanoparticle Pairs: Effect of medium for enhanced nanosensing,” *Nano Lett.*, vol. 8, no. 12, pp. 4347–4352, 2008.

[148] D. Bedeaux and J. Vlieger, *Optical Properties of Surfaces*. Imperial College Press, 2002.

[149] E. P. K. Currie, A. B. Sieval, G. J. Fleer, and M. A. C. Stuart, “Polyacrylic acid brushes: Surface pressure and salt-induced swelling,” *Langmuir*, vol. 16, no. 22, pp. 8324–8333, 2000.

[150] E. Jabbari and S. Nozari, “Swelling behavior of acrylic acid hydrogels prepared by γ-radiation crosslinking of polyacrylic acid in aqueous solution,” *Eur. Polym. J.*, vol. 36, no. 12, pp. 2685–2692, 2000.

[151] S. H. Yuk, S. H. Cho, and H. B. Lee, “pH-sensitivie drug delivery system using O/W emulsion,” *J. Control. Resease*, vol. 37, pp. 69–74, 1995.

[152] K. J. Savage, M. M. Hawkeye, R. Esteban, A. G. Borisov, J. Aizpurua, and J. J. Baumberg, “Revealing the quantum regime in tunnelling plasmonics,” *Nature*, vol. 491, no. 7425, pp. 574–577, 2012.

[153] R. T. McDonough, H. Zheng, M. A. Alila, J. Goodisman, and J. Chaiken, “Optical interference probe of biofilm hydrology: label-free characterization of the dynamic hydration behavior of native biofilms,” *J. Biomed. Opt.*, vol. 22, no. 3, p. 035003, 2017.

[154] L. McLaughlin-Borlace, F. Stapleton, M. Matheson, and J. K. Dart, “Bacterial biofilm on contact lenses and lens storage cases in wearers with microbial keratitis.,” *J. Appl. Microbiol.*, vol. 84, no. 5, pp. 827–838, 1998.

[155] L. Wiley, D. R. Bridge, L. A. Wiley, J. V. Odom, T. Elliott, and J. C. Olson, “Bacterial biofilm diversity in contact lens-related disease: Emerging role of Achromobacter, Stenotrophomonas, and Delftia,” *Investig. Ophthalmol. Vis. Sci.*, vol. 53, no. 7, pp. 3896–3905, 2012.